Soft wearable devices for deep-tissue sensing

Muyang Lin[1,6], *Hongjie Hu*[2,6], *Sai Zhou*[2,6] *and Sheng Xu*[1,2,3,4,5]✉

Abstract | Wearable devices with skin-like mechanical properties enable continuous monitoring of the human body. However, wearable device design has mainly focused on recording superficial signals from the skin thus far, which can only reveal limited information about health and disease. Deep-tissue signals, for example, electrophysiologic, metabolic, circulatory, thermal and mechanical signals, often have stronger correlation with disease and can predict the onset of symptoms. In this Review, we discuss the engineering of soft wearable devices that can sense signals in deep tissues. We highlight electrical, electromagnetic, thermal and mechanical sensing approaches, investigating sensing mechanisms, device designs, fabrication processes and sensing performance, with a focus on penetration depth and temporal and spatial resolutions in the human body. Finally, we discuss remaining challenges in the field and highlight strategies to further improve penetration depth and specificity, accuracy and system-level integration.

Soft wearable devices that can capture physiological signals from the human body can be implemented in healthcare and consumer electronics to support the healthcare ecosystem[1–8]. The skin-like mechanical properties of wearable devices allow intimate and non-restrictive contact with the skin surface, enabling efficient coupling between the device and skin[9,10], thereby, minimizing energy loss at the interface and enhancing physiological signal collection. Furthermore, a tight device–skin interface reduces capacitive coupling of electromagnetic noises and motion artefacts, further improving the signal-to-noise ratio. In addition, non-restrictive contact enables continuous and long-term monitoring[11]. Integrated with intelligent algorithms, the data collected by wearable devices can reveal distinct signal patterns, which may improve our understanding of diseases and allow the prediction of the onset of acute symptoms[12].

Wearable devices can record or derive physiological signals by measuring electrical impedance (for example, skin permeability[13] and hydration[14]), electrochemical potential (for example, sweat composition[4] and pH (REF.[15])), optical absorption (for example, skin colour[16] and arteriole oximetry[17]), thermal distribution (for example, skin temperature[18], sweat rate[19] and superficial perfusion[20]) and mechanical strain (for example, cutaneous pressure[21], respiration[22], skin deformation[23] and skin stiffness[24]). The sensing range of current wearable devices is typically limited to the skin surface or areas close (~mm) to the epidermis. However, such superficial signals do not necessarily reveal the physiological status of internal organs or tissues, including electrophysiology, metabolism, circulation, thermal properties and organ mechanics (FIG. 1). For example, the core body temperature influences metabolic processes[25] and deviations can lead to thermal disorders[26]; however, core body temperature is only loosely correlated with skin temperature measured by typical wearable devices[18]. Indeed, superficial signals are usually manifestations of deep-tissue signals. Signals from centrally located inner organs can provide a systemic view of the entire human body; for example, blood flow in the central aorta indicates the perfusion of organs in the entire body[27], whereas signals from subsurface vessels and capillaries only reflect local perfusions[20]. Therefore, probing deep-tissue signals allows direct and, often, more accurate investigation of human health and disease compared with skin-surface sensing. However, such signals are difficult to capture, owing to strong shielding of integumentary and musculoskeletal systems. Therefore, deep-tissue sensing represents a grand challenge in wearable health monitoring (BOX 1).

In this Review, we discuss important developments in wearable deep-tissue-sensing strategies, including electrical, electromagnetic, thermal and mechanical sensing, focusing on mechanisms, device fabrication (TABLE 1) and key performance metrics. We highlight several examples that can non-invasively detect deep-tissue signals and examine possibilities to improve sensing depth and spatial and temporal resolutions. Finally, we discuss outstanding challenges and outline a roadmap for future developments.

Electrical probes

The human body can be viewed as a sophisticated electrical system consisting of active and passive components. Active components can generate biopotentials[28]

[1]*Department of NanoEngineering, University of California San Diego, La Jolla, CA, USA.*

[2]*Materials Science and Engineering Program, University of California San Diego, La Jolla, CA, USA.*

[3]*Department of Electrical and Computer Engineering, University of California San Diego, La Jolla, CA, USA.*

[4]*Department of Bioengineering, University of California San Diego, La Jolla, CA, USA.*

[5]*Department of Radiology, University of California San Diego, La Jolla, CA, USA.*

[6]*These authors contributed equally: Muyang Lin, Hongjie Hu, Sai Zhou.*

✉*e-mail: shengxu@ucsd.edu*

https://doi.org/10.1038/s41578-022-00427-y

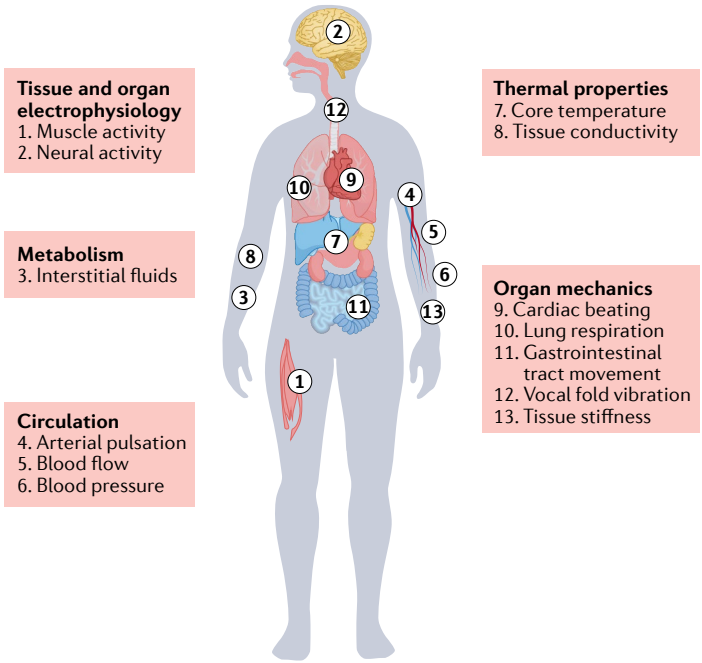

Fig. 1 | **Deep-tissue signals that can be sensed by soft wearable devices.** Five major categories of deep signals (that is, tissue and organ electrophysiology, metabolism, circulation, thermal properties and organ mechanics) can be accessed across the body. Exemplary signals are given in each category.

and passive components conduct biopotentials and can respond to electrical fields from an external source. Therefore, deep tissues can be accessed by applying either passive electrical probes for biopotential recording or active electrical probes for impedance tomography or iontophoresis.

Passive biopotential recording

Electrogenic cells, such as neurons and myocytes, can generate electrical potentials across their cell membranes by changing local ion concentrations in the extracellular fluid through ionic channels. The resulting change in cell membrane polarity leads to the generation of an action potential. The sum of action potentials fired by a group of electrogenic cells forms a local field biopotential, which allows studying brain activities[29], cardiac rhythm[30], muscle performance[31] and gastrointestinal motility[32]. Biopotentials can propagate in the body by a combination of ionic conduction (primarily in biofluids) and electrical polarization (in conductive tissues, including biofluids, and less conductive regions, such as bones and air cavities)[28]. Once biopotential signals reach the skin surface, they can be converted into electric currents using wet, dry, non-contact or microneedle sensors[33,34].

Wet sensors. Wet sensors are widely used in wearable devices and typically consist of a hydrogel layer and a metal electrode to form a wet skin–electrode interface (FIG. 2a). In particular, silver/silver chloride electrodes provide low half-cell potential at the interface (~+220 mV against the standard hydrogen electrode)[35], which introduces a low and stable direct current bias to the recorded biopotential[36]. The hydrous nature of wet sensors enables intimate skin contact, reducing the impedance of the stratum corneum from ~1 MΩ to ~100 kΩ (REF.[37]). However, wet sensors have a limited lifetime and electrode sensitivity substantially decreases if the gel dehydrates.

Dry sensors. Dry sensors do not contain an evaporative hydrogel layer and are, thus, in direct contact with the skin[38] (FIG. 2b), which maximizes the longevity of the electrode. Owing to their durability, dry electrodes are intensively studied in the field. The electrode in dry sensors is typically made of metals or conductive polymers, for example, poly(3,4-ethylenedioxythiophene) polystyrene sulfonate[39], which provides high ionic and electronic mobilities[40] to facilitate signal conversion at the interface. Dry-sensor electrodes commonly rely on natural skin moisture (for example, from perspiration or environmental humidity) to fill the air gaps at the skin–electrode interface and achieve low impedance[37]. Without sufficient interfacial moisture, contact impedance can be as high as hundreds of kΩ. This limitation can be addressed by improving surface contact; for example, nanostructured materials can be applied to increase the interfacial contact area of dry electrodes, thereby, decreasing contact impedance[41,42]. Contact impedance can also be decreased by active sensor designs, for example, by directly integrating an amplifier with the dry sensor. Thereby, signals are buffered before driving the impedance-mismatched back-end circuit, which results in a higher signal-to-noise ratio[37,43]. Alternatively, electrodes can be made of conductive hydrophilic polymers that can absorb sweat, thereby, turning dry interfaces into artificial 'wet interfaces'[44]. Furthermore, dry interfaces offer the opportunity to improve device adhesion to reduce motion artefacts in measurements. In situ-printed electrodes can fill the submillimetre grooves and bumps on the skin surface, forming highly adhesive and ultra-conformal interfaces for motion-tolerant sensing[45].

Non-contact sensors. Non-contact electrodes also provide a dry interface. Non-contact electrodes contain a dielectric layer (for example, a galvanically inactive and chemically inert textile)[46] between the skin and the conductor (FIG. 2c). Biopotentials from the skin can then be extracted by polarizing the dielectric layer[37]. Such an interface passes high-frequency (~hundreds of hertz) components but blocks low-frequency components in the biopotential spectra. Non-contact electrodes have high impedance (for example, ~300 kΩ at 100 Hz)[37] and excessive noise, which makes the recording of low-amplitude signals challenging.

Microneedle sensors. Microneedle sensors can pierce the insulating stratum corneum to contact the conductive dermis directly (FIG. 2d), resulting in high sensitivity[47]. Conductive microneedles can be made with a tip size of ~5 μm and a height of ~30–300 μm by wafer-compatible microfabrication[48,49]. Microneedles embedded in conductive tissues serve as anchors to mechanically secure the sensing interface and, therefore, reduce motion artefacts during recording[47]. However, even though microneedles are deemed minimally invasive, concerns of infection and skin irritation remain.

Penetration depth is not a primary concern in biopotential sensing, because the human body contains >60% water and is, thus, highly conductive. In addition, temporal resolution is high, owing to the fast propagation of biopotentials and the high sampling rate of state-of-the-art analogue-to-digital converters (>1 kHz). By contrast, quantification of spatial resolution is challenging, because biopotentials propagate in tissues isotropically, which causes signal smearing. Therefore, the sources of biopotentials are difficult to resolve by sensors placed on the skin unless the propagation distance is sufficiently short[50]. Biopotential smearing also occurs at the skin–electrode interface, because the electrode does not only pick up signals from areas located directly under the interface but also from its vicinity. Interfacial smearing can be mitigated by decreasing electrode size; however, this strategy is unfavourable for biopotential coupling that requires a larger electrode size to give a stronger signal. Alternatively, a concentric ring electrode can be designed[51] that functions as a physical approximation of Laplacian spatial filters, which calculate the second derivative of the biopotential (Laplacian potential) with high spatial contrast. In practice, this potential derivative can be calculated as weighted ring potential values per unit area (FIG. 2e). Weighted calculation of ring potential values also improves the signal-to-noise ratio at the centre electrode[51]. Here, the calculated potential represents the signal acquired at the electrode centre with a spatial resolution of the ring spacing[52]. For example, a large concentric electrode with an outer ring diameter of ~24 mm and a ring spacing of 6 mm could confine the measured biopotential signals within a radius of 6 mm (REF.[51]) (FIG. 2e), therefore, biopotential smearing at the skin–electrode interface can be controlled.

Box 1 | **Challenges in deep-tissue sensing**

Electrical pulses, thermal energy and mechanical movements are constantly generated in the body. These signals can be directly recorded by passive sensing. By contrast, active sensing requires the transmission of an external signal (electrical, electromagnetic, thermal or mechanical), whose interaction with tissues is then detected. In deep-tissue sensing, the sensor does not directly interact with the target tissue, which poses several challenges, in particular, regarding penetration depth, spatial resolution and temporal resolution.

Penetration depth

The human body dampens signals during transmission, which greatly limits probing depth. Electric fields diminish owing to impedance and the screening effect of tissues and organs; electromagnetic waves are strongly absorbed by tissues; thermal conduction can be interfered by ambient temperature fluctuations and shielded by thermally insulating adipose tissues; mechanical waves can be reflected and scattered by tissue interfaces.

Spatial resolution

Most signals propagate isotropically in tissues and, thus, signals received at the surface may come from multiple sources. In addition, signal smearing from deflection and reflection during propagation is inevitable. Therefore, spatial specificity, that is, differentiating signals from individual sources, remains challenging.

Temporal resolution

Acquiring signals from deep tissues is not always an instant process. Although the establishment of electrical fields is instantaneous, the migration of charged molecules in electrical fields, transmission of electromagnetic pulse sequences, conduction of heat and propagation of mechanical waves take time. Therefore, temporal resolution is limited, in particular, if the measured signals are labile.

Active electrical impedance tomography

Active electrical impedance tomography (EIT) maps conductivity and permittivity distributions. Here, an array of electrodes is attached to the skin and a pair of electrodes applies quantified low-magnitude alternating currents that travel through the body during measurement. The resulting potential distributions on the skin surface are recorded by the other electrodes in the array (FIG. 2f). The complex impedance of the human body, which is dependent on its conductivity and permittivity, can then be derived from the real and imaginary parts of the recording. This process is repeated multiple times by applying alternating currents on different electrode pairs in the array, enabling the reconstruction of a 2D tomographic image. Deep tissues or organs, such as the lung[53], heart[54], breast[55] and brain[56], have different concentrations of free ions and, thus, specific impedances, which are shown as clear contrasts on the tomogram[57].

The spatial resolution of EIT is limited[58], because recovering the conductivity and permittivity of deep tissues from surface measurements is an ill-posed, nonlinear inverse problem[57]. Slight noise in the measured data causes a substantial deviation in the image reconstruction. Moreover, the electric currents in EIT travel in 3D along the pathways of the least impedance, but not in linear pathways as X-ray in computed tomography. Therefore, currents that leave the plane in which the electrodes reside cannot be captured, which results in more than one solution to the reconstruction of the 2D tomographic image projected from a 3D volume. The imaging quality of EIT can be improved by optimizing the reconstruction algorithms and the recording electrodes.

EIT images can be reconstructed by stochastic or deterministic algorithms[58]. The stochastic algorithm depends on probabilistic statistical reasoning[59] to reduce the relative error between each solution candidate of the inverse problem. To solve the inverse problem, artificial intelligence methods and evolutionary computational techniques inspired by natural evolution and biological systems have been exploited. The deterministic algorithm can be linear or nonlinear. EIT reconstruction is a nonlinear problem, and, thus, linear techniques are typically first applied to linearize the model, followed by regularization to prevent overfitting[58,60]. However, such linear approximation is difficult for the reconstruction of complex geometries or high contrasts. Nonlinear techniques generally search for the best conductivity distribution model that minimizes the difference between the applied potentials from the inverse problem and the calculated potentials from the forward problem. Nonlinear methods result in a smaller error and exhibit a higher spatial resolution than linear methods[58]. However, to obtain the best nonlinear model, complex and time-consuming computation is required, resulting in low temporal resolution.

The electrode substantially affects the image quality in EIT reconstruction. EIT mainly uses the adjacent excitation mode[61], and traditional electrode design only allows each electrode to function for either excitation or measurement. To improve imaging quality and reveal more information in the reconstruction, a compound

Table 1 | **A summary of deep-tissue sensing strategies**

Principle		Sensing mechanisms	Fabrication approaches	Research trends
Electrical	Biopotential propagation	Potentials produced and conducted by the body are measured to derive electrical activities of tissues	Wet electrodes: thermal gelation[230] Dry electrodes: layered coating[51] Microneedles: wet etch[231], 3D printing[34], maskless photolithography[48] Anode/cathode: sputtering[232], chemical vapour deposition[72], electron beam deposition[77] General patterning: laser cutting[230], mould casting[39], inkjet printing[233], screen printing[74], photolithography[77], reactive ion etching[77]	Improving spatial resolution through electrode pattern design[51]; improving interfacial adhesion for low impedance[42]; reducing motion artefacts[45]
	Electrical impedance tomography	Conductivity and permittivity distribution of a body section is mapped based on the current flow induced by electrodes		Developing customized model or introducing machine learning[58] to increase reconstruction accuracy and temporal resolution; customizing electrode microstructure[64] and configuration[71] to increase signal-to-noise ratio and spatial resolution
	Reverse iontophoresis	Interstitial fluid is extracted from deep tissues by electro-osmotic flow under an applied electric field		Reducing time for reverse iontophoresis[75]; increasing osmotic pressure in deep tissues[77]; improving ion mobility of the skin[13]; increasing sensing depth[77]
Electromagnetic	Radiofrequency transmission	The resonance frequency of the antenna is measured to determine the tissue's dielectric properties; data and power are transmitted	Antenna fabrication: screen printing[89], inkjet printing[90], embroidery[91]	Improving penetration depth by manipulating the transmission phase and field[105]; designing transient implanted coils to avoid surgical removal[98,234]
	Optical illumination	Photophysical interactions with chromophores inside human cells are measured to provide biometric information	Light emitters: micromachining[117], spin coating[125] Waveguides: mould casting[235], photolithography[236], spin coating[237], laser writing[238]	Developing progressive micromachining techniques to minimize wearable laser systems; integrating soft and biodegradable waveguides to increase sensing depth[128]
Thermal	Thermal conduction	Thermal exchange at the skin surface is quantified to measure the core body temperature	Metal thermistor/heater: electron beam deposition[133,142] Interconnect patterning: photolithography[133,142], reactive ion etching[135] Thermal insulators: mould casting[146], spin coating[142]	Improving thermal insulation to reduce response time[146]
	Thermal modulation	Thermal conductivity is derived from the temperature response of heated tissues		Improving accuracy of conductivity measurement[133]
Mechanical	Vibration	Passive vibration: vibrations are monitored inside the human body through mechanical waves propagation	Passive and active vibration sensors: sol–gel[156], electron beam deposition[166], transfer printing[155], chemical vapour deposition[164], micromachining[239], electrospinning[159] General patterning: photolithography[166], wet etching[156], reactive ion etching[155], laser ablation[162]	Passive vibration: differentiating signals with overlapped frequency ranges by optimizing the system design[162] and advanced signal processing techniques[165]; improving durability and sensitivity of soft electronic stethoscopes[159]
		Active vibration: vibrators deform tissues; sensors detect the change in tissue strain		Active vibration: improving axial resolution by applying multiple vibrators[155]; improving temporal resolution by consecutive sampling during vibration process[155]
	Ultrasonography	Amplitude mode and brightness mode: ultrasound reflections are measured at the interfaces with acoustic impedance mismatch	Transducer assembling: mould casting[170], dicing and filling[176], micromachining[180] Interconnect patterning: laser ablation[176], screen printing[214]	High-frequency arrays[169]; advanced imaging techniques, such as harmonic imaging[169]; mapping positions on irregular surfaces[203]; integrating acoustic metamaterials with wearable transducers[171]
		Doppler mode: frequency change of reflected/scattered ultrasound waves is measured to derive tissue motion and flow		
		Quasi-static elastography: ultrasound reflection at tissue interfaces is measured before and after compression to quantify tissue mechanics		

electrode design can be implemented, including an outer electrode for current injection and an inner electrode for voltage measurement[62]. Using more electrodes can increase spatial resolution; however, with a large number of electrodes and small spacing, currents can travel through the paths on the surface layer to adjacent electrodes, which considerably reduces the currents flowing into the body, limiting sensing depth[62]. Therefore, a balance between the electrode number and spacing should be maintained. Similar considerations should be given to the electrode size. A large electrode can reduce the skin–electrode contact impedance, which improves sensitivity, but at the cost of spatial resolution, because the surface covered by the electrode is treated equipotential. Wet electrodes with evaporative hydrogels are not ideal for reliable long-term monitoring. By contrast, dry electrodes provide more stable contact impedance and are, thus, widely used in EIT. Materials with high sensitivity in dry electrodes can improve EIT imaging quality. In particular, nanostructures (for example, nanotubes[63] and nanofibres[64]) and highly conductive materials[65] (for example, metals and carbon-based materials) in the electrode can reduce contact impedance and improve sensitivity. For example, a silver-plated polyvinylidene fluoride nanofibre electrode can improve electrode conformability with the skin and reduce contact impedance[64], resulting in a high signal-to-noise ratio and high reconstruction accuracy.

In addition to algorithm and electrode optimization, time-difference EIT and multi-frequency EIT can be applied to improve the spatial resolution of reconstructed images. Time-difference EIT characterizes the changes in tissue impedance over time, which reduces inaccuracies caused by interpersonal differences in anatomy, insufficient skin–electrode contact or circuit design. Time-difference EIT is particularly suitable for signals that require dynamic monitoring, such as respiration[66] (FIG. 2g) and perfusion[67], whereas signals that barely change over time fall into the static background. In multi-frequency EIT, alternating currents of multiple frequencies are simultaneously applied. As the resonant frequency and impedance spectrum differ in each tissue owing to different cellular structures and compositions, multi-frequency EIT can maximize the contrast between tissues and has, thus, been widely used in monitoring brain and breast tumour sizes[55,68].

Owing to computational complexity, in 2D EIT, images are reconstructed by assuming 2D current flows; however, in reality, currents flow in 3D. Increasing computing power has enabled 3D EIT, in particular, for imaging deep-organs, such as the brain[56] and lung[69]. 3D EIT reconstructs volumetric images based on 3D current flows from the entire surface of the object[70], which results in a higher accuracy than 2D EIT. 3D EIT is based on several assumptions: the target has an ideal geometrical shape; the electrodes are placed around the body part in well-defined positions; and all electrodes have the same contact impedance. However, in practice, these assumptions do not hold true; in particular, if the subject moves during imaging, the results are disturbed. Therefore, electrode placement configuration is crucial for the quality of image reconstruction, with different configurations demonstrating distinct characteristics. For example, a zigzag configuration tolerates minor spacing errors but performs poorly in the presence of noise[71]; a square configuration provides fewer image artefacts than a zigzag configuration but is vulnerable to spacing errors[71]. Therefore, configurations should be carefully selected based on the specific needs in different scenarios.

Active reverse iontophoresis

Reverse iontophoresis allows non-invasive extraction of interstitial fluids from the intercellular matrix, up to 25 mm under the skin surface[72,73]. Under an applied electric field, ions are drawn from the interstitial fluid and migrate through the skin driven by Coulomb forces, forming an electroosmosis flow[4,74]. Positive and negative ions can then be extracted at the cathode and at the anode, respectively. As the skin contains negative charges[75], positive ions have a higher mobility in skin than negative ions[76], and, thus, the net flow of ions follows the direction of positive ions (from the anode to the cathode). Biomarkers in the interstitial fluid, including electrolytes (for example, sodium, phosphate, magnesium, potassium and calcium), metabolites (for example, glucose, alcohol, lactate and cortisol) and small amounts of large molecules (for example, proteins, nucleic acids, neuropeptides and cytokines)[4,74], migrate along the net ionic flow to the skin surface (FIG. 2h).

Reverse iontophoresis has three main limitations. First, the low temporal resolution of ~0.003 Hz (REF.[75]) hinders real-time applications. Modest skin permeability creates barriers for ion diffusion at the skin–electrode interface[13]. In addition, the natural osmotic pressure in interstitial fluid is low, and, thus, ion migration is slow, which leads to reabsorption of the interstitial fluid by blood vessels, reducing the amount of fluid that can be extracted[77]. Therefore, extracting biomarkers at a concentration sufficiently high for analytic testing takes time. Temporal resolution can be improved by using microneedles to break the diffusion barrier of the skin, which improves ion mobility[78]. Microneedles further functionalized with biorecognition components can also selectively capture target biomarkers to increase extraction efficiency[79,80]. Alternatively, voltage can be applied to increase skin permeability. High-voltage electric pulses applied to the stratum corneum cause the temporary formation of conducting pores in skin cell membranes, which allows surrounding molecules to easily pass through[81]. To increase the osmotic pressure of the interstitial fluid, stimulants, such as hyaluronic acid having a high density of positive charges, can be added at the anode. The stimulants are then transdermally driven into the tissue by iontophoresis[77] (FIG. 2i), which prevents reabsorption by vessels, increases the flux and shortens the extraction time of interstitial fluid. Increasing electrode sensitivity can further reduce the amount of interstitial fluid needed for biomolecular detection. For example, modifying a carbon working electrode with glucose oxidase and Prussian blue allows quantitative sensing of glucose by amperometry at very low concentrations[75].

Second, reverse iontophoresis suffers from low spatial resolution, primarily owing to the large footprint

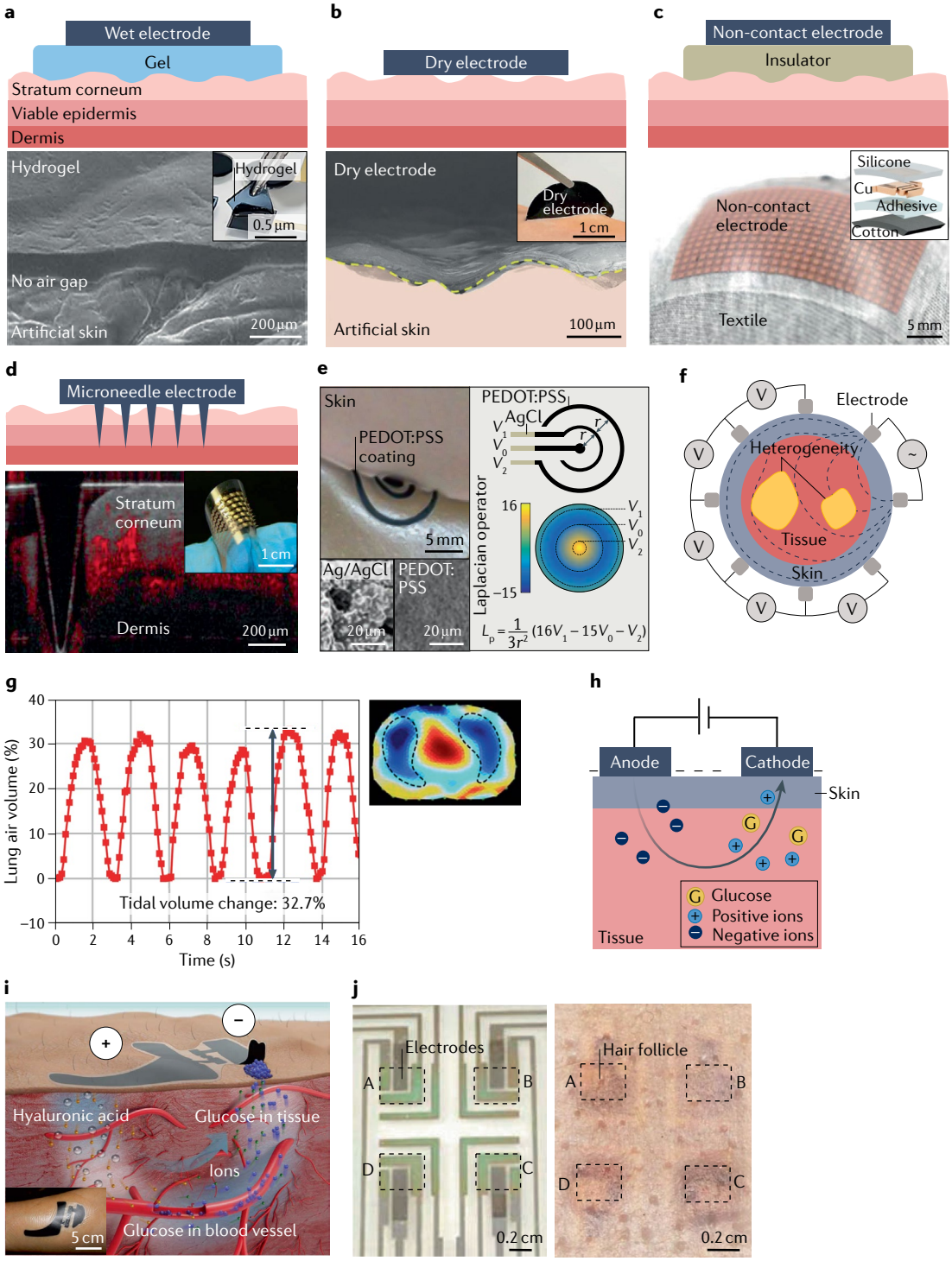

of electrodes. The major interstitial fluid outlets are hair follicles[72], and a large electrode allows fluid collection from a great amount of hair follicles; however, it also covers sweat glands. The indiscriminate collection of biomolecules from both reverse iontophoresis and perspiration reduces sensing accuracy. To solve this problem, an array of miniaturized sensors can be used[72], in which each sensor element only covers a single hair follicle (FIG. 2j). The loss in electrode area can be compensated by increasing electrode sensitivity, for example, using graphene films decorated with platinum nanoparticles, which allows high sensing accuracy and spatial resolution (~10 mm to ~2 mm)[72,77].

Third, reverse iontophoresis has a maximum penetration depth of ~25 mm (REFS[72,73]), and the composition of interstitial fluid extracted from this range only has a weak correlation with the central arterial blood, in particular, if the biomolecule concentration is highly dynamic[82]. Furthermore, the >40 kΩ impedance of subcutaneous tissues prevents the Coulomb force from pulling ions from deep tissues. Increasing the drive voltage can increase extraction depth but can also induce severe

◀ Fig. 2 | **Electrical probes. a** | Wet skin–electrode interface (top) and scanning electron microscope image of a wet electrode mounted on artificial skin (bottom). Inset: optical image of tissue-like ultrasoft hydrogel[230]. **b** | Dry skin–electrode interface (top) and scanning electron microscope image of a dry electrode mounted on artificial skin (bottom). Inset: optical image of an organic dry electrode[39]. **c** | Non-contact textile electrode interface (top) and optical image of a non-contact electrode integrated in cotton fabric (bottom). Inset: structure of the electrode-impregnated textile[46]. **d** | Microneedle skin–electrode interface (top) and optical coherence tomography image of a microneedle array applied on human skin[243] (bottom). Inset: optical image of a flexible microneedle array[244]. **e** | Optical image of a conformal concentric electrode (top left) and scanning electron microscope images of a Ag/AgCl electrode and poly(3,4-ethylenedioxythiophene) polystyrene sulfonate (PEDOT:PSS) coating (bottom left). Schematics of a three-lead concentric biopotential electrode and intensity distribution of the Laplacian operator (right). The equation shows the calculation of Laplacian potential (L_p) as a function of three ring potentials (V_0, V_1 and V_2) and ring spacing (r)[51]. **f** | Electrical impedance tomography for deep-tissue sensing. **g** | The conductivity distribution of the right and left lungs during inspiration and expiration (right). Average resistivity of the right and left lungs over time[66] (left). **h** | Reverse iontophoresis principle. **i** | Major processes in reverse iontophoresis. Hyaluronic acid penetrates the skin to increase the interstitial osmotic pressure, glucose permeation and interstitial fluid transport. Inset: optical image of an ultrathin skin-like electrode[77]. **j** | Optical images showing a 2 × 2 array electrode for extracting and sensing interstitial fluid (left) and tested skin (right). Each electrode of the array can cover one hair follicle, which improves sensing specificity[72]. Panel **a** is adapted with permission from REF.[230], AAAS. Panel **b** is adapted from REF.[39], CC BY 4.0 (https://creativecommons.org/licenses/by/4.0/). Panel **c** is adapted from REF.[46], Springer Nature Limited. Panel **d** is adapted from REF.[243], CC BY 4.0 (https://creativecommons.org/licenses/by/4.0/); inset in panel **d** is adapted from REF.[244], CC BY 4.0 (https://creativecommons.org/licenses/by/4.0/). Panel **e** is adapted with permission from REF.[51], Wiley. Panel **g** is adapted with permission from REF.[66], Elsevier. Panel **i** is adapted with permission from REF.[77], AAAS. Panel **j** is adapted from REF.[72], Springer Nature Limited.

skin irritations[74]. Alternatively, thermal activation can decrease the impedance of subcutaneous tissues and promote skin permeability[13]. Skin can also be pretreated with low direct current voltage or high-voltage pulses for 30 min before reverse iontophoresis, which induces pores in the epidermis and reduces skin resistance to ~1 kΩ, thereby, increasing the extraction depth[83].

Electromagnetic probes

The human body emits electromagnetic waves at infrared wavelengths owing to the thermal radiation effect[84]. These electromagnetic waves cannot be directly captured for deep-tissue sensing, because the signals are superimposed by infrared radiation of superficial tissues[85]. Deep tissues can, however, be probed by actively transmitting electromagnetic waves into the human body. Typically, radiofrequency (~3 kHz to 300 GHz) and optical frequency (~300 GHz to 3,000 THz) bands can be used. The short wavelength and high frequency of electromagnetic waves enable sensing with high spatial-temporal resolutions.

Active radiofrequency transmission

Radiofrequency can be directly sensed using antennas (FIG. 3a); here, the resonance frequency of the antenna is measured, which is dependent on tissue permittivity, which, in turn, is determined by the composition and temperature of the tissue[86,87]. Permittivity varies between different tissue types and also as a result of dynamic changes in tissue composition. For example, arterial pulses can change the blood volume in arteries, resulting in a periodical change in overall arterial permittivity[88] (FIG. 3b). At a given composition, tissue permittivity also negatively correlates with tissue temperature[87]. Therefore, changes in deep-tissue composition or temperature are reflected by the measured shift in resonance frequency of the antenna. Multiple fabrication approaches have been adopted to optimize antenna architecture, including screen printing[89], inkjet printing[90] and embroidery[91]. Wearable antennas can record a suite of deep-tissue signals, including blood flow[92], tissue temperature[93] and biomolecular concentration[94].

However, radiofrequency resonance sensing is limited by low measurement accuracy. The shift in resonance frequency is not only sensitive to parameters that can alter tissue permittivity, but is also affected by the geometry of wearable antennas[95]; in practice, it is almost impossible to isolate individual contributing factors. Moreover, radiofrequency resonance sensing is an indirect approach, and, therefore, requires calibrations[93]. The accuracy of pre-measurement or post-measurement calibration can also be unreliable, owing to temporal fluctuations of tissue parameters.

Radiofrequency can also be measured by coupling a wearable radiofrequency antenna with an implantable sensor (permanent[96,97] or biodegradable[98]). Sensing is then achieved by passive resonance or backscattering modulation[99]. In both scenarios, the wearable antenna initiates radiofrequency wave transmission and the implanted device responds and returns deep-tissue signals. Passive resonance sensing is based on the radiofrequency resonance between the wearable antenna and the implantable device[97,98] (FIG. 3c). The wearable antenna scans the frequency band to determine the shift in resonance frequency of the implanted device, typically that is, of the capacitive device component[97,98], which reveals tissue parameters (FIG. 3d,e).

In backscattering modulation, the wearable antenna delivers radiofrequency power to the implanted device, which senses tissue parameters and transmits data in a modulated reflection. The data are then received and demodulated by the wearable antenna[99] (FIG. 3f). The implanted device has an active coil whose backscattering characteristics are altered by the collected signals. The signals are coded as modulated wave frequencies or amplitudes, and, thus, signal loss during propagation is minimized[100]. Of note, the backscattering configuration also allows radiofrequency communication and energy transfer, enabling the implantable device to realize controllable actuations[101].

Passive resonance can achieve deeper tissue penetration than backscattering modulation, owing to only moderate radiofrequency signal loss in tissues[102]. Resonance sensing of tissue temperature has been demonstrated for tissues up to 5 cm below the skin[93]. By contrast, the penetration depth of backscattering modulation is limited by the implanted coil size, which is typically below 1 cm in diameter[99]. Coupling between the wearable antenna and the implanted coil occurs in the near-field regime, and, therefore, their distance has to be smaller than the coil size for strong coupling[99]. Increasing the size or power of the wearable antenna can increase the coupling distance[101,103,104]; however, form factor and power budgets of the antenna may be limiting factors. Alternatively, the antenna can be designed into

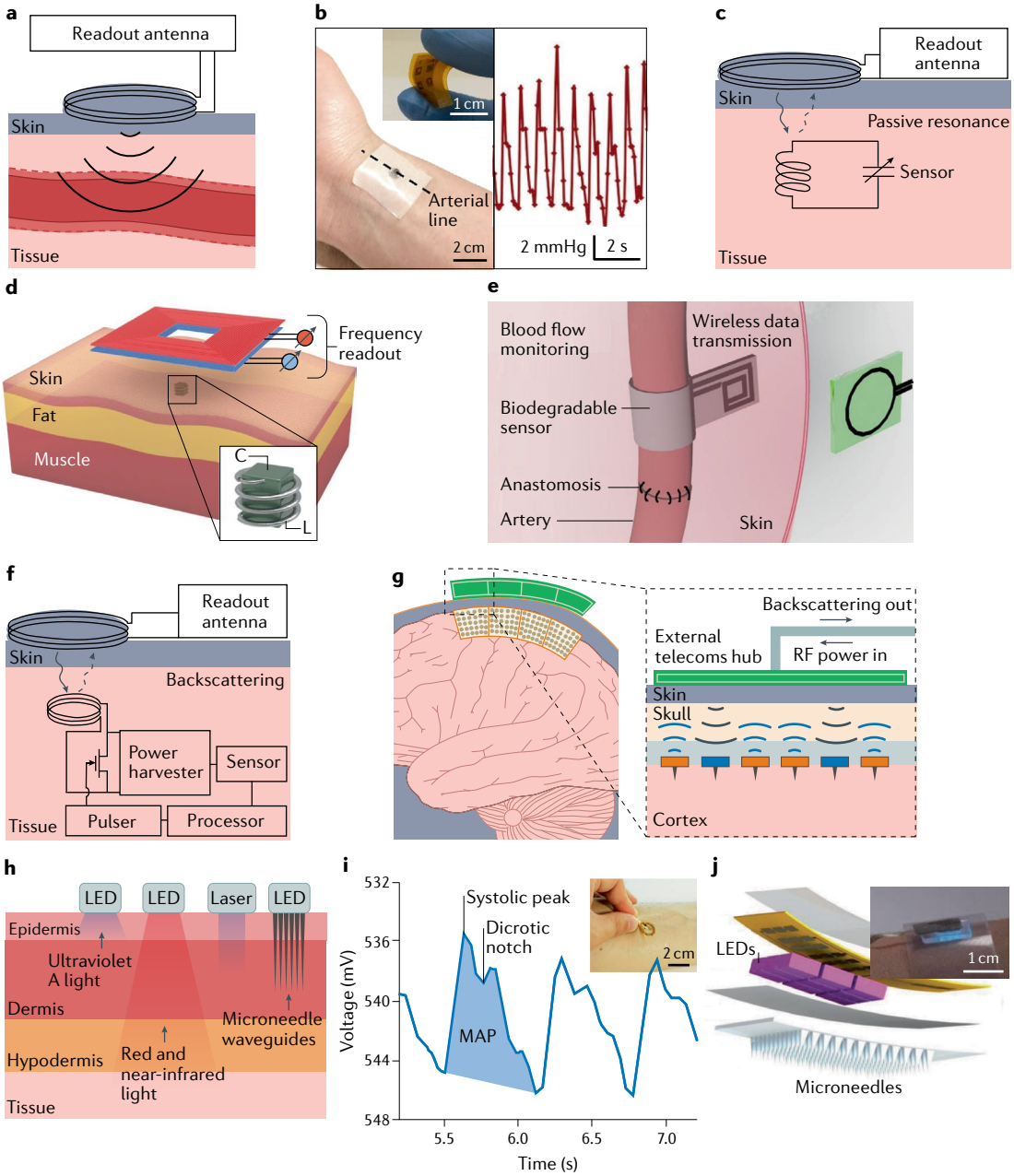

Fig. 3 | **Electromagnetic probes. a** | Resonance sensing using a wearable antenna. **b** | Monitoring of the arterial pulse using an electromagnetic antenna. Inset: optical image of a flexible antenna array[88]. **c** | Electromagnetic sensing based on an implanted passive inductor–capacitor (LC) resonator. **d** | Electromagnetic sensing by passive resonance. Inset: zoomed-in view of the passive LC resonance sensor[97]. **e** | Sensing of blood flow by passive resonance[98]. **f** | Electromagnetic sensing based on an implanted backscattering modulation device. **g** | Electromagnetic sensing by backscattering modulation sensors[106]. **h** | Optical sensing depths at different light wavelengths and light sources, and with or without waveguide materials. **i** | Mean arterial pressure (MAP) measurement by photoplethysmography. Inset: optical image of the device on the forearm while pinched[120]. **j** | Structure of a wearable optical device with an array of ultraviolet A light-emitting diodes (LEDs) and an array of poly(lactide-*co*-glycolide acid) microneedle waveguides. Inset: optical image of the device on the skin[118]. RF, radiofrequency. Panel **b** is adapted from REF.[88], Springer Nature Limited. Panel **d** is adapted from REF.[97], Springer Nature Limited. Panel **e** is adapted from REF.[98], Springer Nature Limited. Panel **g** is adapted with permission from REF.[106], IEEE. Panel **i** is adapted from REF.[120], CC BY 4.0 (https://creativecommons.org/licenses/by/4.0/). Panel **j** is adapted with permission from REF.[118], Wiley.

a metasurface, with subwavelength features, to engineer transmission phases and field patterns, extending the coupling to the mid-field regime[105].

Backscattering modulation has a better spatial resolution than passive resonance. In backscattering modulation, spatial resolution is determined by the size of the implanted sensor, which can be miniaturized to <1 mm (REFS[97,106]) (FIG. 3g). In passive resonance sensing, the measurement can only reflect an average of the tissue parameter, because radiofrequency transmission is

omnidirectional. Phased-array antennas delivering a focused beam could address this limitation[107].

The antenna frequencies of both passive resonance and backscattering modulation are in the kHz–GHz range, which is fast enough to capture changes in typical tissue signals, such as pulse[92], glucose content[94] and oxyhaemoglobin saturation[108], which are typically at frequencies of <10 Hz. Therefore, sensing has high bandwidth and fidelity.

Active optical illumination

Light transmitted to the body undergoes photophysical interactions with chromophores inside cells. By illuminating a target area and recording the reflected light, biometric information can be obtained, such as the perfusion status[109], tumour grade[110] and neural activities[111]. Light intensity is attenuated by absorption and scattering in tissues, and most photons can only access the epidermis and dermis (within a depth of ~3 mm)[112]. Melanin and haemoglobin are thought to dominate light absorption in the epidermis and dermis, respectively[112]. Melanin has a broad absorption spectrum[113], whereas the absorption spectrum of haemoglobin contains three distinct peaks that span across the blue to green-yellow regions[114], allowing optical sensing of haemoglobin content and, thus, change of blood volume (for example, in photoplethysmography)[115]. Glucose in biofluids has strong absorption at near-infrared wavelengths and can, therefore, be sensed by diffuse reflectance spectroscopy[116].

In addition to absorption, scattering by particulates substantially contributes to light attenuation. This forms the basis of laser Doppler flowmetry, which can be implemented in wearable devices[117] to measure the Doppler frequency shift caused by red-blood-cell scattering in capillaries to derive blood flow. However, scattering disperses light in three dimensions, which weakens the incident intensity at the target tissue and introduces noise from off-target tissues, thereby, reducing the overall sensitivity. The primary source of particulate scattering in the skin are filamentous proteins, such as keratins in the epidermis and collagens in the dermis. In addition, melanosomes in the epidermis, cell nuclei, cell membranes and many other structures with dimensions similar to the wavelength of light contribute to scattering[114].

Absorption and scattering enable optical sensing; however, they are also barriers for deep-tissue sensing, which can be addressed by optimizing the light source. The wavelength of light determines the sensing depth, because the absorption spectra of skin chromophores depend on the wavelength[2]. Thus, optimizing the wavelength can minimize absorption and maximize penetration depth. Red or near-infrared light (600–1,350 nm wavelength) has a higher penetration depth (>3 mm) in tissues[2] than ~100 μm for ultraviolet A light (320–400 nm wavelength)[118] (FIG. 3h). Photoplethysmography devices based on red and near-infrared light can measure heart rate[119,120], respiration rate[121], blood pressure[120] (FIG. 3i) and peripheral oxygen saturation[109]. Green light (492–577 nm wavelength) can also be used for photoplethysmography. Green light has stronger haemoglobin absorption than red and near-infrared light, increasing the sensitivity[115]. Furthermore, green radiation from the environment shows less interference and, thus, background noise is low. However, the shallow penetration depth (~0.5 mm)[122] of green light limits applications to near-skin tissue sensing.

The light source can be non-directional (light-emitting diodes) or directional (lasers). The light-emitting diode can be a point source, for example, a micro-light-emitting diode[123], or a flexible and stretchable plane emitter, such as an organic light-emitting diode[124,125]. Owing to high divergence and low intensity, most photons from light-emitting diodes are typically absorbed and scattered within 3 mm from the skin surface[2]. By contrast, lasers are coherently amplified light beams with very low divergence and high intensity, which enables deeper penetration (>5 mm)[126]. For example, a highly directional laser beam can be used to obtain feedback with high sensitivity and accuracy from red blood cells without disturbing the flow field[117].

Optical waveguides can further be integrated with the light source to deliver light to specific sites with minimal attenuation[127] (FIG. 3h). To be compatible with wearable devices, waveguide materials should be flexible, biocompatible and biodegradable[128]. For example, biodegradable hydrogels can be designed with excellent optical properties, such as polyethylene-glycol-based hydrogels, which are transparent and can be optimized for low signal intensity loss (0.17 dB cm^{-1}) in the blue-green range[129]. In addition, the waveguide structure can be optimized; for example, arrayed microneedle waveguides made of poly(lactide-*co*-glycolide) are transparent in the ultraviolet region and can redistribute light into tissues >1 mm in depth with minimal damage to the skin[118] (FIG. 3j).

Thermal probes

Cells constantly generate heat owing to cellular respiration, which is then conducted within the body and exchanged with the environment. Heat generation and conduction, which are modulated by thermoregulation processes, also determine the core temperature of the body, reflecting the metabolic rate, as well as the health and function of tissues[130–132]. In addition to core temperature, tissue thermal conductivity can reveal physiological information, including the level of hydration[133], perfusion[134] and healing[135]. The thermal properties of deep tissues can be probed by passive or active thermal conduction, and by active thermal modulation.

Passive and active thermal conduction

Measuring thermal conduction at the skin surface can reveal thermal energies and properties in deep tissues, with shorter conduction paths resulting in higher measurement accuracy. Wearable thermal sensing strategies usually aim at measuring the core body temperature, which is normally kept stable by thermoregulation[136,137]. By contrast, the skin surface constantly exchanges heat with the environment, which causes frequent changes in skin temperature. Traditionally, thermistors are inserted into natural body orifices to directly access the core temperature[138]. Alternatively, wearable skin temperature sensors can quantify the difference between the

core temperature and the skin temperature, for example, using the dual-heat-flux approach or the zero-heat-flux approach.

In the dual-heat-flux approach[139], two thermistor–insulator pairs[140] are used to quantify the heat gradient in the insulator layer to derive the core temperature, based on Fourier's law of thermal transmission[141] (FIG. 4a). This measurement principle is implemented in passive thermal conduction sensors, which feature a thermal insulator, usually made by foam materials with a high void fraction (for example, polyurethane foam). Their porous structure ensures low thermal conductivity and high flexibility[142] (FIG. 4b).

In the zero-heat-flux approach, a thermal insulator is applied to the skin surface to minimize heat loss to the environment. In case of an ideal thermal insulator, heat loss to the environment is zero, which is equivalent to the scenario in deep tissue (that is, the insulator is equivalent to a thick tissue layer covering the target area). Therefore, the temperature measured on the skin surface in the target area represents the core temperature. In reality, an ideal thermal insulator does not exist. Therefore, an electronic heater can be applied to compensate for heat loss, which constitutes an active thermal-conduction-sensing strategy. The added heat is controlled by the temperature difference between two thermistors on both sides of the thermal insulator (FIG. 4c,d). This closed-loop system eventually reaches equilibrium, resulting in a near-zero-heat-flux condition, so that the core temperature can be acquired (FIG. 4e). Active zero-heat-flux sensors have been shown to perform equally well as the clinical standard (nasopharyngeal probe)[131], achieving a standard error of <0.5 °C (REF.[143]). Using this approach, temperature can be measured up to 10 mm below the skin[144].

However, heat-flux sensing of deep-tissue temperature is only accurate for small depths, because the fat under the skin is an effective thermal insulator. Therefore, subcutaneous fat layers thicker than >9 mm considerably reduce measurement accuracy[138]. Furthermore, temporal resolution is low. In active core temperature sensing, the time to reach thermal equilibrium can be as long as 15 min at room temperature[138], and passive devices have an even longer response time. The response time can be reduced by improving thermal insulation materials and device structures; for example, a nylon–glass fibre composite shell filled with frustum-shaped polydimethylsiloxane[145] or bilayers of metal and phase-change materials can be applied[146] (FIG. 4f). The spatial resolution of heat-flux sensing is also limited. Spatial resolution does not exist in the axial direction, because the model treats deep tissue as an isothermal bulk, and lateral resolution is proportional to the device size. Typically, owing to the influence of the edge–centre temperature gradient, the device is larger than 25 mm (REF.[138]). The gradient can be reduced by adding a thermally conducting shell, which enables a smaller device size[141].

Active thermal modulation

By actively modulating the heat applied to the skin surface, the thermal conductivity of deep tissues can be derived[133]; here, the response to modulated heating is recorded based on the 3ω method[147]. Such devices usually contain a resistive heater, an alternating current source and a voltmeter (FIG. 4g,h). A sinusoidal current at 1ω frequency is then applied to the heater, causing its temperature to oscillate at a frequency of 2ω, owing to Joule heating. The resistance of the heater changes with the temperature at a frequency of 2ω, which leads to oscillation of the voltage output that contains a 3ω component influenced by heat dissipation of the underlying tissue[148]. Therefore, temperature oscillation and, thus, tissue thermal conductivity can be derived by measuring the 3ω component in the voltage output[133–135] (FIG. 4i).

However, a limitation of the 3ω method is that penetration depth and temporal resolution are both frequency-dependent. A high frequency benefits temporal resolution, but reduces the thermal penetration depth to several millimetres[135]. In addition, the measured conductivity has limited spatial resolution. The heat modulation process is associated with uncontrollable heat transfer to surrounding tissues, and, therefore, the 3ω method can only generate the average conductivity of the skin and deep tissues.

Mechanical probes

Passive or active mechanical sensing can capture deep-tissue movements. Vibrations in deep tissues generate mechanical waves that propagate through the body (FIG. 5a), which can reveal characteristics of physiological activities, such as opening and closing of the heart valve (~10 cm depth)[149,150], movement of the gastrointestinal tract (~2 cm depth)[151], contraction of skeletal muscles (~1 cm depth)[152] and vibration of the vocal fold (~1 cm depth)[153,154]. The mechanical waves from deep tissues can be measured with wearable passive sensors. To measure tissues that cannot generate mechanical waves, an external load can be applied to study their mechanical responses, which is the principle of active mechanical sensing[155,156]. Human tissues are considered viscoelastic materials and, thus, mechanical signals are dampened when travelling in tissue.

Passive and active vibration sensing

Passive vibration sensing has been demonstrated with electronic stethoscopes and accelerometers. Deep-tissue vibrations reaching the skin surface can be probed by an electronic stethoscope through vibrations of its diaphragm and converted into electrical signals by piezoelectric or triboelectric materials with high electromechanical conversion efficiency[157,158]. Wearable stethoscopes can be designed with nanostructured materials; for example, a nanofibrous electronic stethoscope exhibits high sensitivity at a low-frequency range of 10–500 Hz, enabling seismocardiography recordings with a high signal-to-noise ratio[159] (FIG. 5b). The sensor consists of a layer of polyvinylidene fluoride nanofibres sandwiched between two nanofibre electrodes. Gaps (5–15 μm in thickness) between the ultrathin electrodes induce resonance, which greatly increases vibration amplitude and, thus, device sensitivity. However, their ultrathin structure makes these wearable devices fragile, possibly compromising long-term reliability[159].

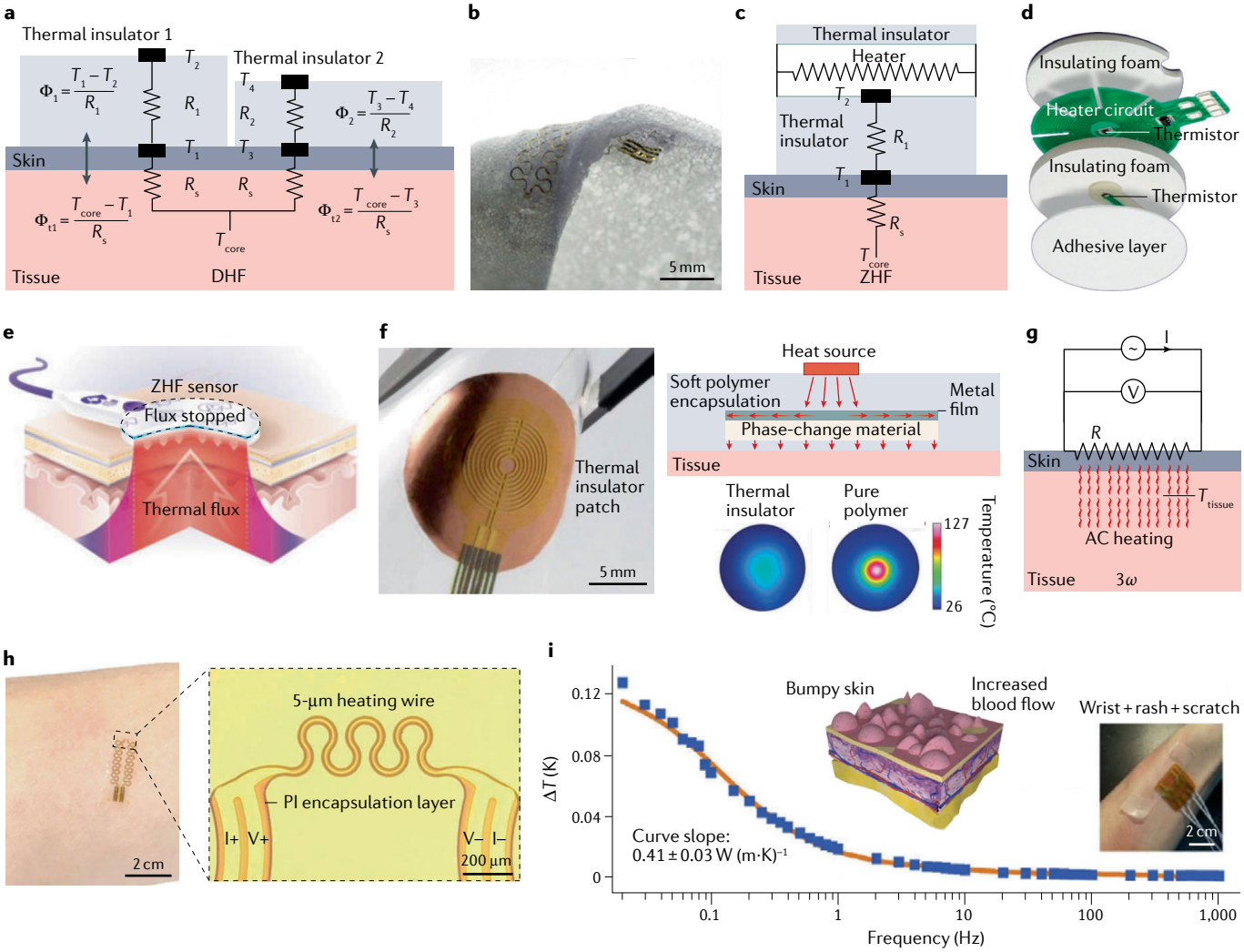

Fig. 4 | **Thermal probes. a** | Dual-heat-flux (DHF) core temperature sensing. The heat flux leaving the tissue (Φ_{t1} and Φ_{t2}) is considered equal to that entering the thermal insulators (Φ_1 and Φ_2). When the heat flux becomes steady ($\Phi_{t1} = \Phi_1$; $\Phi_{t2} = \Phi_2$), the deep-tissue temperature (T_{core}) can be derived as a function of thermistor readings (T_1, T_2, T_3, T_4), thermal resistance in tissue (R_s) and in insulators (R_1, R_2). **b** | Optical image of a polyurethane foam used as a thermal insulator[142]. **c** | Zero-heat-flux (ZHF) core temperature sensing. The heat flux in tissue (with thermal resistance R_s) to the thermal insulator (with thermal resistance R_1) reduces to zero when the temperatures measured by the thermistor pair (T_1 and T_2) become equal. **d** | Multilayered ZHF sensor from 3M Bair Hugger for heat flux control and core body temperature monitoring[242]. **e** | ZHF condition achieved by an active thermal insulation patch. **f** | Optical image of a flexible patch for thermal insulation, achieved by material design (left). The functional composite achieves a thermal barrier. The metal film improves heat dissipation along the in-plane direction and the phase-change material stores the heat during its phase transition (top right). The thermal insulation performance of the functional composite is shown, compared with that of a pure polymer layer as insulator[146] (bottom right). **g** | 3ω sensor for thermal conductivity measurements. Alternating current (AC) is applied to generate modulated heat in tissues, and voltage oscillation at 3ω is recorded for thermal conductivity calculations. **h** | Optical image of a stretchable 3ω sensor on the forearm. Zoomed-in optical image of the sensor shows a serpentine gold heater and polyimide (PI) encapsulation layers[133]. The PI encapsulation separates electrodes for current supply (I+/I–) and voltage recording (V+/V–). **i** | Temperature change (ΔT) as a function of thermal modulation frequency. The thermal conductivity can be derived by fitting the curve[134]. Insets: skin with rash after scratching, which increases blood flow and thermal conductivity (left); optical image of a 3ω sensor on the wrist with rash after scratching (right). Panel **b** is adapted with permission from REF.[142], Wiley. Panel **f** is adapted with permission from REF.[146], Wiley. Panel **h** is adapted with permission from REF.[133], Wiley. Panel **i** is adapted with permission from REF.[134], Elsevier.

Compared with electronic stethoscopes, accelerometers are more robust, allowing long-term operation. In an accelerometer, the inertia of a mass during vibration deforms a piezoelectric material, producing a voltage proportional to the inertial force and converting the acceleration into an electrical signal. Accelerometers offer large bandwidths (0–10 kHz)[160] and high temporal resolution (1–20 kHz)[161], and, thus, they can capture multiple vibrations simultaneously. For example, a skin-mounted accelerometer can record body orientation (~0.1 Hz), swallowing (~0.1 Hz), respiration (~0.3 Hz), cardiac activities (~1–10 Hz) and vocal-fold vibrations (>100 Hz)[162] (FIG. 5c). In addition, device designs featuring an island-bridge structure endow accelerometers with stretchability, allowing them to seamlessly conform to the skin surface[163]. However, electronic stethoscopes and accelerometers have difficulties distinguishing vibrations from different origins if they overlap in the frequency range. A potential solution is to combine multiple vibration sensors at different

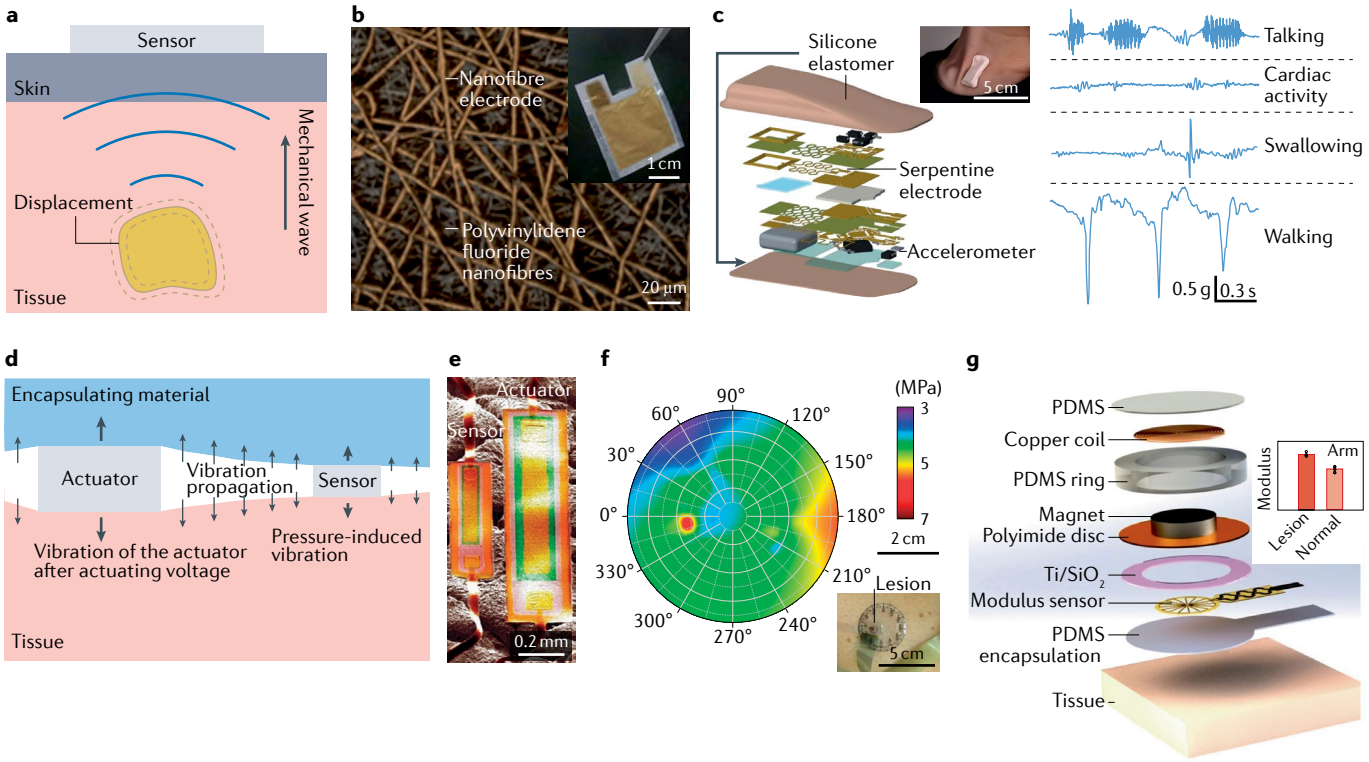

Fig. 5 | **Vibration probes. a** | Passive vibration sensor for tissue motion monitoring. **b** | Microscopic image of a vibration sensor based on nanofibre electrodes and polyvinylidene fluoride nanofibres. Inset: optical image of a fully assembled vibration sensor[159]. **c** | Structure of a soft encapsulated accelerometer (left). Inset: optical image of the device mounted on the suprasternal notch during head rotation. The time series show data of talking, cardiac activity, swallowing and walking recorded by the device[162] (right). **d** | Active vibration sensor for tissue stiffness measurement. Vibration propagates from the actuator along the tissue and encapsulation material to the sensor. **e** | Scanning electron micrograph of a piezoelectric active vibration system on an artificial skin surface[156]. **f** | Tissue stiffness mapping results achieved by a piezoelectric active vibration system. The lesion in the lower leg appears as a high-stiffness region (shown as a red circle) compared with the surrounding healthy tissue. Inset: optical image of the device on the leg[156]. **g** | Structure of an electromagnetic-based active vibration system. Inset: measurements of skin lesion on the arm[155]. PDMS, polydimethylsiloxane. Panel **b** is adapted with permission from REF.[159], PNAS. Panel **c** is adapted from REF.[162], Springer Nature Limited. Panels **e** and **f** are adapted from REF.[156], Springer Nature Limited. Panel **g** is adapted from REF.[155], Springer Nature Limited.

auscultation locations[162,164]. Moreover, advanced signal processing techniques, such as independent component analysis[165], could be applied.

An active vibration sensor is composed of an actuator, which generates mechanical vibrations, and a sensor, which detects deformations in tissues in response to vibrations[155] (FIG. 5d). Compared with the passive approach, active vibration sensing has a smaller sensing depth[156] and a lower temporal resolution[155], but can be applied to organs that do not vibrate spontaneously. Active vibration sensing is typically based on the piezoelectric effect[156,166] or on electromagnetic force[155,167]. In piezoelectric-based sensing, piezoelectric materials vibrate in an oscillating electric field for both actuating and sensing[156]. For example, a conformal piezoelectric system can be applied to characterize soft tissue stiffness[156] (FIG. 5e). Here, the tissue conducts and couples the vibrations sent from the actuator, and the voltage recorded by the sensor reveals the mechanical properties of the tissue[156] (FIG. 5f). This device has a high lateral resolution (~0.5 mm), because it contains miniaturized actuators and sensors. However, owing to the low vibration energy of the actuators, the penetration depth is restricted to the submillimetre range.

In electromagnetic-based sensing, a magnetic material is used as the actuator, vibrating in an oscillating electric field. For example, a miniaturized wearable strain-sensing system has been designed based on electromagnetic force[155] (FIG. 5g). Here, an actuator made of a nickel-coated neodymium magnet in a copper coil delivers controllable pressure to the tissue underneath, and a thin strain gauge picks up the response. Compared with piezoelectric-based sensing, this method induces a higher vibration amplitude, which increases the penetration depth to ~8 mm. This active vibration system can provide rapid quantitative diagnosis of tumours and skin diseases[155], and can also be designed as a wireless haptic interface for virtual and augmented reality applications[167].

The penetration depth of active vibration sensors remains limited. Owing to the viscoelastic nature of human tissues, vibrations generated by the small actuating force are dampened. Increasing the actuator size and input voltage can intensify vibrations. Alternatively, vibrations can be enhanced by modulating the voltage, for example, by adding a direct current bias or by increasing the driving power through replacing the sine wave driving voltage with a square wave[155]. Moreover, active vibration systems have a limited axial resolution,

measuring only the average elastic modulus of the tissue in the target region. Axial resolution can be improved by using multiple vibrators with different sensing depths[155]. Finally, active vibration systems have a low temporal resolution (~5 Hz)[155]; signals are captured only after the tissue has fully recovered from deformation[155], which takes time, owing to the viscoelastic nature of tissues[168].

Active ultrasonography

Ultrasonography is a special form of active vibration sensing, with driving frequencies in the 20 kHz to 200 MHz range[169]. Ultrasound waves can propagate in tissues with little damping and bounce back when encountering tissues with different acoustic impedances; the reflected waves then carry anatomical and mechanical information of deep tissues. Compared with other mechanical probing modalities, ultrasonography has larger penetration depths and higher spatial and temporal resolutions. Owing to low absorption and backscattering, ultrasound can penetrate over a decimetre into human tissues[169] (FIG. 6a). With a working frequency in the megahertz range and wavelengths in the range of hundreds of microns in tissues, ultrasound-based approaches can resolve objects at the submillimetre scale[169].

In ultrasound systems, transducers generate and receive ultrasonic waves. Transducers are often made of piezoelectric materials with a high electromechanical coupling coefficient[169]. A backing layer, typically made of metal–epoxy composites, absorbs excess ultrasound waves, dampens the ringing effect and shortens the

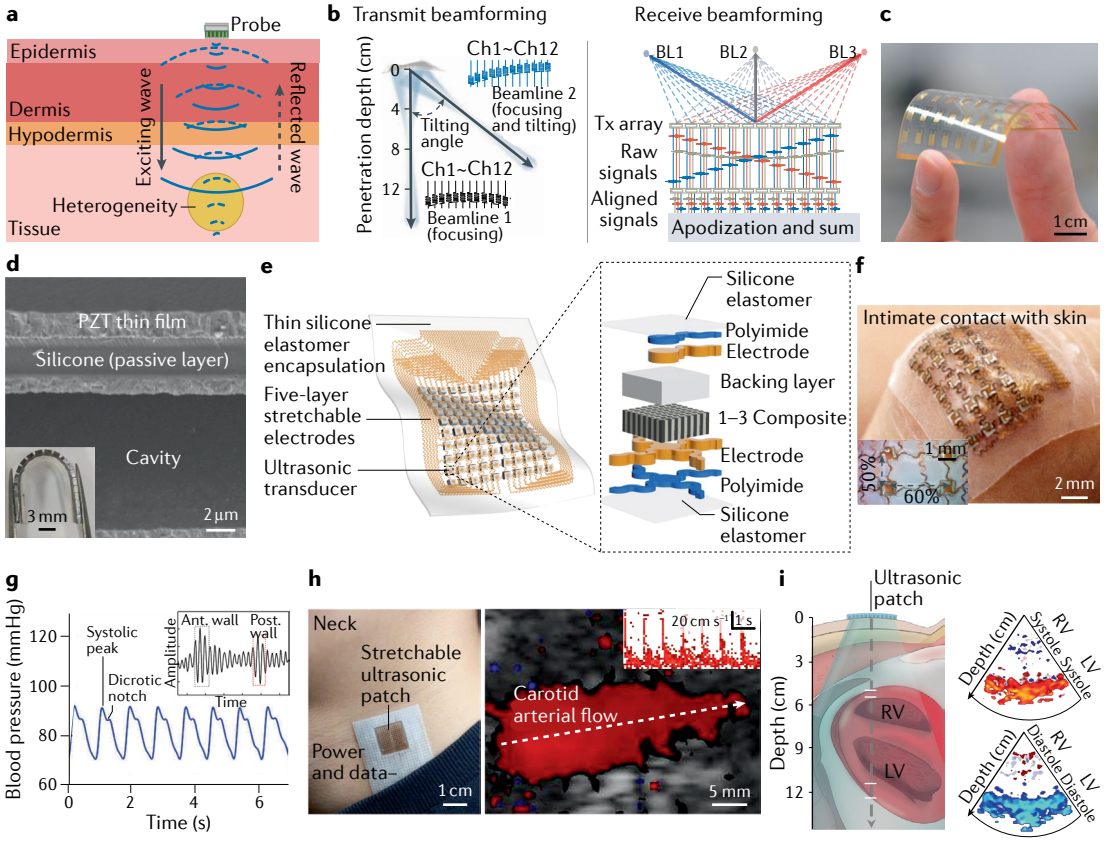

Fig. 6 | **Ultrasonic probes. a** | Ultrasound sensing mechanism for the detection of various deep-tissue signals. **b** | Transmit beamforming (left) and receive beamforming[173] (right) can substantially improve penetration depth and spatial resolution. **c** | Optical image of a flexible capacitive micromachined ultrasonic transducer[180,182]. **d** | Scanning electron micrograph of the unit structure of a piezoelectric micromachined ultrasonic transducer[183]. Inset: optical image of a flexible piezoelectric micromachined ultrasonic transducer array under bending[184]. **e** | Stretchable ultrasonic array (left) and structure of each transducer element[170] (right). **f** | Optical image showing the conformability of a stretchable ultrasonic array on a finger joint with highly irregular skin surfaces. Inset: optical image showing biaxial tensile testing of the device with a stretchability of up to 60% in the *x* direction and 50% in the *y* direction without failure[176]. **g** | Blood pressure waveforms measured from the carotid artery[176]. Inset: received ultrasonic signals with two echo peaks from the anterior (Ant.) and posterior (Post.) blood vessel walls[176]. **h** | Optical image of a stretchable ultrasonic array on a human neck (left). Colour Doppler image of the carotid artery (right) and corresponding flow spectra[173] (inset). **i** | Ultrasonographic window used in cardiac activity monitoring (left). Doppler spectra of the ventricles, showing the systole and diastole of the right ventricle (RV) and left ventricle (LV) (right). Red colour indicates tissue movement towards the device and blue colour indicates movement away from the device[173]. BL, beamline; Ch, channel; PZT, lead zirconate titanate; Tx, transducer. Panel **b** is adapted from REF.[173], Springer Nature Limited. Panel **c** is adapted from REF.[180], CC BY 4.0 (https://creativecommons.org/licenses/by/4.0/). Panel **d** is adapted from REF.[183], CC BY 4.0 (https://creativecommons.org/licenses/by/4.0/), and from REF.[184], Springer Nature Limited. Panel **e** is adapted from REF.[170], CC BY 4.0 (https://creativecommons.org/licenses/by/4.0/). Panels **f** and **g** are adapted from REF.[176], Springer Nature Limited. Panels **h** and **i** are adapted from REF.[173], Springer Nature Limited.

spatial pulse length, thereby, improving spatial resolution in the axial direction[170]. A matching layer, commonly made of composites[169] or metamaterials[171], can compensate for the mismatch of acoustic impedance between the device and the human body to enhance ultrasonic transmission, which increases penetration depth. The electrical impedance mismatch between the transducer, power source and data acquisition systems also needs to be considered, because it reduces power transmission efficiency and signal-to-noise ratio. An impedance-matching circuit can be used to adjust the transducer's electrical impedance to match that of the back-end instrument[172] and to improve the sensitivity and signal-to-noise ratio of the system.

A single transducer produces a very broad beam, leading to low spatial resolution, which can be addressed by beamforming strategies using arrayed transducer elements. In transmit beamforming[173] (FIG. 6b, left), multiple elements can be programmed to transmit ultrasonic waves synergistically. In-phase waves can be superimposed to form a focal point with intensified acoustic energy. A focused ultrasound beam improves the spatial resolution and penetration depth of the device[173]. Receive beamforming allows post-processing of echo signals to achieve a synthetic focusing effect and improve spatial resolution[173] (FIG. 6b, right). In the transducer element array, the pitch and aperture size are crucial for device performance. Keeping the pitch within half a wavelength can suppress grating-lobe-based artefacts and reduce the blurring effect at the sensing target when steering the ultrasound beam[169]. In addition, increasing the aperture size narrows the beam, leading to a smaller focal point. These strategies can be applied to increase lateral resolution[169].

Seamless contact between the device and skin is also important in ultrasonography to allow efficient energy transmission at the interface. When used alone, conventional rigid ultrasound probes have limited acoustic coupling[174,175]. Ultrasonic couplants can be applied to resolve this issue; however, they can affect user experience, in particular, for long-term use. Furthermore, the presence of excess couplants can result in a high-pass-filtering effect on ultrasonic signals, causing the loss of small signals, which decreases the signal-to-noise ratio[170]. To overcome this challenge, flexible and stretchable ultrasound devices have been designed that provide tight contact with the skin without couplants, enabling wearable applications[173,176–179].

Flexible ultrasonic sensors can be made of intrinsically flexible piezoelectric polymers[179] or micromachined ultrasonic transducers[180]. Piezoelectric polymers have an acoustic impedance that matches that of human tissues and, thus, they have a broad bandwidth, which makes them outstanding ultrasound receivers[181]. However, they are not ideal for transmission owing to their low piezoelectric coefficient d_{33} (REF.[181]), low dielectric constants[169] and high dielectric loss[181]. Micromachined transducers rely on the bending motion of a thin membrane, enabling a thin device profile and flexibility, but at the cost of electromechanical coupling properties. Both capacitive and piezoelectric micromachined transducers have been designed. In capacitive micromachined transducers[180,182] (FIG. 6c), a membrane is attracted by an electrostatic force; the mechanical restoring force of the membrane resists deformation, which limits the vibration amplitude and, thus, the energy conversion efficiency. In piezoelectric micromachined transducers, a bilayer unimorph structure[183,184] (FIG. 6d) is composed of an active piezoelectric layer, working in d_{31} mode to provide actuation, and a passive layer, creating strain asymmetry along the thickness of the device. The passive layer cannot convert mechanical energy into electrical energy nor vice versa[185], which compromises device sensitivity.

Flexible ultrasonic arrays can bend over developable surfaces (for example, a cylindrical surface)[186–188]; however, the human body surface is nondevelopable, which can lead to gaps between the arrays and the skin. Alternatively, stretchable ultrasonic arrays[132,170,173,176] can better adapt to the surface of the human body. Stretchable ultrasonic arrays are designed by integrating high-performance piezoelectric materials with an island-bridge structure. The islands are then interconnected by serpentine-shaped metallic bridges, followed by encapsulation in thin elastomers[170] (FIG. 6e). The serpentine conductive network offers >50% biaxial stretchability with minimal impact on transducer performance, enabling intimate contact with nondevelopable surfaces[176] (FIG. 6f).

Stretchable ultrasonic devices can capture various deep-tissue signals. For example, a single transducer in the amplitude mode can derive the blood pressure waveform from blood vessel diameters, based on the reflected wave patterns from the anterior and posterior walls of the blood vessel[176] (FIG. 6g). The temporal resolution of these devices is ~120 Hz, determined by the pulse repetition frequency of reconstructing a complete blood pressure waveform. This resolution is sufficient for capturing blood pressure variations[176]. The lateral resolution depends on the resonant frequency and the size of the transducer, whereas the axial resolution depends on the resonant frequency and bandwidth[189]. With a transducer size of $0.9 \times 0.9\ mm^2$, a resonant frequency of 7.5 MHz and a −6 dB bandwidth of 32%, the lateral and axial resolutions are 0.9 mm and 0.4 mm, respectively[176]. The amplitude mode can further reveal the thickness and morphology of muscle for muscle contraction monitoring[179], gesture recognition[190] and force estimation of the forearm[191].

In brightness mode, an ultrasonic array could be used for 2D or 3D imaging of discontinuities inside a structural component[170], with a temporal resolution of ~30 Hz (REF.[192]), which is attributed to the complex beamforming process. The lateral resolution depends on the pitch and the aperture size of the array, whereas the axial resolution depends on the frequency and bandwidth of the array elements[193]. With a one-wavelength pitch, 10.7-wavelength aperture, 47% −6 dB bandwidth and 3.5 MHz resonant frequency, a stretchable ultrasonic transducer array provides 0.8 mm lateral resolution and 0.6 mm axial resolution[170].

In Doppler mode, the velocity of tissue movement can be captured by the Doppler effect, measured by a stretchable ultrasound sensor[173,194]. By measuring the frequency shift caused by red blood cells, their flow velocity and

direction can be determined and visualized[173] (FIG. 6h). In addition, tissue Doppler images can reveal ventricular wall motions[173] (FIG. 6i). Here, the temporal resolution is in the range of tens of hertz, owing to the beamforming processes[173]. The lateral resolution of Doppler mode is the same as in brightness mode; however, the axial resolution is less (2.5 mm), owing to the long transmit pulses needed to accurately demodulate the frequency shift[173].

Quasi-static elastography could also be potentially integrated in wearable platforms. In this mode, ultrasound waves are first transmitted to determine the location of scattering sources in a tissue. A mild uniaxial compression (~0.5–1% strain) is then applied to the tissue, and the resulting phase shifts of signals are collected. Finally, cross-correlation[195], least-squares strain estimator[196] and inverse elasticity problem[197] algorithms are applied to the signals before and after compression to derive the displacement, strain and Young's modulus of each point in the tissue. Quasi-static elastography can be used to characterize the mechanical properties of tissues, similar to active vibration methods. However, this approach has greater penetration depths (>5 cm)[198] than active vibration (~8 mm)[155], and higher axial resolution (hundreds of micrometres)[199] than active vibration (over a millimetre)[155], owing to the short wavelength of ultrasound. Quasi-static elastography also has a higher temporal resolution (tens of hertz)[200] than active vibration (~5 Hz)[155], because signal phase shifts can be continuously detected, without the need to wait for the recovery of deformations. The high temporal resolution of quasi-static ultrasound elastography makes it suitable for various applications, including real-time monitoring of myocardium stiffness[201] and muscle stiffness during rehabilitation exercises[202].

To improve the spatial resolution and penetration depth of stretchable ultrasonic arrays, materials, and fabrications need to be designed to enable high frequency, fine pitch, wide aperture and large bandwidth. Moreover, harmonic imaging, based on the transmission of low-frequency ultrasound waves and the receiving of higher harmonic frequencies[169], can be explored for stretchable ultrasonic platforms. Using this technique, both high penetration depth and high spatial resolution could be achieved. In addition, accurate beamforming requires information on the position of each transducer element, which is challenging to achieve in dynamic movements. Positions could be mapped by exploiting time reversal of the ultrasonic field[203] or strain sensing[187]. Time reversal could correct the phase aberration of the array and determine a proper time delay profile for beamforming[203]. Strain sensors could be integrated with the wearable ultrasonic array to measure array geometry to compensate for time delay[187].

Wearable ultrasonic devices can also power and communicate with implanted devices for deep-tissue sensing and data transmission[204]. Ultrasound waves can transfer mechanical energy into deep tissue, which can be converted to electrical power by a piezoelectric transducer in an implant[205] that senses deep-tissue signals, such as temperature[206], local oxygenation[205] or organ pressure[207]. The collected deep-tissue signals can then be converted into digital data by a time-to-digital converter, modulated by a finite-state machine and transmitted to the wearable ultrasonic device by an implanted piezoelectric transducer[208]. In addition, ultrasound can deliver therapy to deep tissues[209,210], providing a pathway to wearable, closed-loop, monitoring-therapeutic devices.

Outlook

The different physical sensing approaches, discussed in this Review, enable non-invasive or minimally invasive deep-tissue sensing, albeit with distinct sensing resolutions and penetration depths (TABLE 2). Next-generation deep-tissue-sensing technologies will require improvements in penetration depth and specificity, accuracy and system-level integration.

Penetration depth and specificity

Signal smearing typically increases with sensing depth, which creates a dilemma in sensor development, in particular, if the goal is a closed-loop system for diagnosis and therapy[211]; here, penetration depth is crucial for data acquisition and specificity is often required to guide therapy. Hybridized sensing strategies using multiple modalities can achieve higher penetration depth and

Table 2 | **Depth and spatial-temporal resolutions of deep-tissue-sensing methods**

Method	Depth (mm)	Spatial resolution (mm)	Temporal resolution (Hz)	Refs
Biopotential recording	~1–50	~6–50	~10^2–10^4	29–32,39,41,44–48,51,52
Electrical impedance tomography	~0–150	~1–10 (depending on pixel size)	~10–10^3	54,61,64
Reverse iontophoresis	Subcutaneous tissue (estimated depth: ~0–25)	~2–10	~2×10^{-3}–3×10^{-3}	72,75,77
Radiofrequency transmission	~0–40	~5–50	~5×10^2–1.5×10^4	88,92,93,97,98,106,108,240
Optical illumination	~0–5	~1–10	~10–10^4	2,118,241
Thermal conduction	~0–20	25	~1×10^{-3}–3×10^{-3}	131,142,242
Thermal modulation	~0–3	NA	~1×10^{-3}–1	133–135
Vibration sensing	~0–100	~0.5–100	~5–2×10^4	155,156,161,162
Ultrasonography	~5–140	~0.3–0.8	~30–1.2×10^2	173,176,187,192

NA, not applicable.

specificity simultaneously. In particular, ultrasonography is a highly versatile approach in terms of hybridization with other sensing modalities[212,213]; for example, radiofrequency radiation and optical illumination could excite tissues to generate ultrasound waves, which can then be picked up by piezoelectric transducers. Combining these excitation and sensing processes enables thermoacoustic and photoacoustic sensing. For example, wearable photoacoustic imaging devices allow deep-tissue imaging at micrometre–millisecond spatiotemporal resolutions, while maintaining centimetre-level penetration depths. Here, acoustics enable deep penetration and the optics component generates biomolecular contrast with high resolution[132,214]. Long-term functional imaging of chemical signals in deep tissues further complements the physical signals, generating a holistic picture of the physiological status of the human body[132].

Accuracy

In deep-tissue sensing, signal acquisition suffers from degradation in fidelity and noise coupling in the signal propagation path. Inaccuracies and measurement errors can be introduced by many factors, including displacement of sensors, movement of target tissues or confounding signals from adjacent tissues. In active sensing approaches, sensing accuracy can be improved by modulated transmissions. In particular, by activating the sensor with an encoded sequence, transmitting and receiving processes are encrypted and random noise and artefacts can be differentiated and rejected from the coded signals. Therefore, loss in signal fidelity is greatly reduced. Encoded transmission has been applied in EIT[215], electromagnetic transmission[98], thermal modulation[133], active vibration[155] and ultrasonography sensing[173]. Here, simple encoding, for example, oscillating at a fixed or nearly fixed frequency[92,176], substantially increases sensing accuracy as compared with non-modulated sensing approaches. More complex sequences, such as a binary phase-encoded pulse sequence[216], could further increase accuracy, because they can deliver more energy to the tissue, which increases the signal-to-noise ratio[217]. In addition, complex sequences are easier to distinguish from noise.

Machine-learning-based filtering algorithms can also aid in rejecting noises and artefacts, and in classifying signals to improve sensing accuracy. The continuous and great amount of data acquired by wearable devices can contribute to the data pool to optimize machine learning algorithms, which further increases signal analysis accuracy[218]. For example, genetic algorithms[219] and mathematic optimization[32] have been explored as filters to reduce the noise in biopotential signals.

System-level integration

Most sensors developed for deep-tissue sensing remain at a proof-of-concept stage and are wired to complex supporting components[220]. To enable deep-tissue sensing in a real-world environment, wireless system-level integration is required, which is not a trivial task. The power consumption of the device must be well controlled to expand device lifetime. Moreover, the integrated system should be non-restrictive to human activities, so the device should be sufficiently small to induce only minimal mechanical load to the skin, or the device should be sufficiently soft to conform to the skin surface.

To become small, miniaturization relies on the development of application-specific integrated circuits that contain analogue-to-digital converters, amplifiers and filters, which have to be integrated with the sensors to achieve a small form factor; for example, integrated circuits have been designed for biopotential sensing[221] and ultrasonography imaging[222]. Miniaturization also reduces power consumption, and integrated circuits are typically at the sensing front-end, which benefits the signal-to-noise ratio by amplifying signals before noise is coupled. To become soft, circuits can be constructed by adopting an island-bridge structure[5,170] to enable device stretchability. Using a multilayered integration strategy[31], such a stretchable circuit can have a component and function density similar to traditional rigid printed circuit boards. Alternatively, soft materials can be used to achieve component-level softness and flexible or stretchable circuit designs[223,224].

Wireless communication can be achieved by electromagnetic waves, for example, through Bluetooth[31], Wi-Fi[225] or radiofrequency identification[98,226,227]. Furthermore, metasurfaces enable the manipulation of the amplitude, phase and polarization of electromagnetic wavefronts[228] to reduce power consumption and increase the data rate and security of wireless communication[228,229].

Deep-tissue signals reveal important information about health and disease; however, deep-tissue sensing is only beginning to be explored with soft wearable devices. Strategies to enhance penetration depth, spatial resolution and temporal resolution have enabled deep-tissue sensing with wearables, enriching the toolbox of clinical researchers. The development of wearable sensors for near-skin-surface sensing has progressed at speed, and we anticipate similar advances in deep-tissue sensing. The power of wearable electronics is yet to be uncovered — there is plenty of room under the skin.

Published online 14 March 2022

1. Ray, T. R. et al. Bio-integrated wearable systems: a comprehensive review. *Chem. Rev.* **119**, 5461–5533 (2019).
2. Lee, G.-H. et al. Multifunctional materials for implantable and wearable photonic healthcare devices. *Nat. Rev. Mater.* **5**, 149–165 (2020). **This review discusses multifunctional materials and healthcare applications for wearable optical sensors**.
3. Someya, T. & Amagai, M. Toward a new generation of smart skins. *Nat. Biotechnol.* **37**, 382–388 (2019).
4. Kim, J., Campbell, A. S., de Ávila, B. E.-F. & Wang, J. Wearable biosensors for healthcare monitoring. *Nat. Biotechnol.* **37**, 389–406 (2019).
5. Wang, C., Wang, C., Huang, Z. & Xu, S. Materials and structures toward soft electronics. *Adv. Mater.* **30**, 1801368 (2018).
6. Ates, H. C., Yetisen, A. K., Güder, F. & Dincer, C. Wearable devices for the detection of COVID-19. *Nat. Electron.* **4**, 13–14 (2021).
7. Quer, G. et al. Wearable sensor data and self-reported symptoms for COVID-19 detection. *Nat. Med.* **27**, 73–77 (2021).
8. Mishra, T. et al. Pre-symptomatic detection of COVID-19 from smartwatch data. *Nat. Biomed. Eng.* **4**, 1208–1220 (2020).
9. Kim, D. H. et al. Epidermal electronics. *Science* **333**, 838–843 (2011).
10. Lim, H. R. et al. Advanced soft materials, sensor integrations, and applications of wearable flexible hybrid electronics in healthcare, energy, and environment. *Adv. Mater.* **32**, 1901924 (2020).
11. Gambhir, S. S., Ge, T. J., Vermesh, O., Spitler, R. & Gold, G. E. Continuous health monitoring: an opportunity for precision health. *Sci. Transl Med.* **13**, eabe5383 (2021).
12. Jung, J., Lee, J., Lee, J. & Kim, Y. T. A smartphone-based U-Healthcare system for real-time monitoring of acute myocardial infarction. *Int. J. Commun. Syst.* **28**, 2311–2325 (2015).
13. Pu, Z. et al. A thermal activated and differential self-calibrated flexible epidermal biomicrofluidic

device for wearable accurate blood glucose monitoring. *Sci. Adv.* **7**, eabd0199 (2021).
14. Huang, X., Yeo, W.-H., Liu, Y. & Rogers, J. A. Epidermal differential impedance sensor for conformal skin hydration monitoring. *Biointerphases* **7**, 52 (2012).
15. Anastasova, S. et al. A wearable multisensing patch for continuous sweat monitoring. *Biosens. Bioelectron.* **93**, 139–145 (2017).
16. Inamori, G. et al. Neonatal wearable device for colorimetry-based real-time detection of jaundice with simultaneous sensing of vitals. *Sci. Adv.* **7**, eabe3793 (2021).
17. Kim, J. et al. Miniaturized battery-free wireless systems for wearable pulse oximetry. *Adv. Funct. Mater.* **27**, 1604373 (2017).
18. Gao, L. et al. Epidermal photonic devices for quantitative imaging of temperature and thermal transport characteristics of the skin. *Nat. Commun.* **5**, 4938 (2014).
19. Nyein, H. Y. Y. et al. A wearable patch for continuous analysis of thermoregulatory sweat at rest. *Nat. Commun.* **12**, 1823 (2021).
20. Webb, R. C. et al. Epidermal devices for noninvasive, precise, and continuous mapping of macrovascular and microvascular blood flow. *Sci. Adv.* **1**, e1500701 (2015).
21. Dagdeviren, C. et al. Conformable amplified lead zirconate titanate sensors with enhanced piezoelectric response for cutaneous pressure monitoring. *Nat. Commun.* **5**, 4496 (2014).
22. Yang, S. et al. "Cut-and-paste" manufacture of multiparametric epidermal sensor systems. *Adv. Mater.* **27**, 6423–6430 (2015).
23. Wang, Y. et al. Wearable and highly sensitive graphene strain sensors for human motion monitoring. *Adv. Funct. Mater.* **24**, 4666–4670 (2014).
24. Zhao, Y. et al. Highly sensitive flexible strain sensor based on threadlike spandex substrate coating with conductive nanocomposites for wearable electronic skin. *Smart Mater. Struct.* **28**, 035004 (2019).
25. Landsberg, L., Young, J. B., Leonard, W. R., Linsenmeier, R. A. & Turek, F. W. Do the obese have lower body temperatures? A new look at a forgotten variable in energy balance. *Trans. Am. Clin. Climatol. Assoc.* **120**, 287–295 (2009).
26. Leon, L. R. & Helwig, B. G. Heat stroke: role of the systemic inflammatory response. *J. Appl. Physiol.* **109**, 1980–1988 (2010).
27. Chaudhry, R., Miao, J. H. & Rehman, A. *Physiology, Cardiovascular* (StatPearls, 2020).
28. Buchner, T. On the physical nature of biopotentials, their propagation and measurement. *Physica A* **525**, 85–95 (2019).
29. Mahmood, M. et al. Fully portable and wireless universal brain–machine interfaces enabled by flexible scalp electronics and deep learning algorithm. *Nat. Mach. Intell.* **1**, 412–422 (2019).
30. Xu, S. et al. Soft microfluidic assemblies of sensors, circuits, and radios for the skin. *Science* **344**, 70–74 (2014).
31. Huang, Z. et al. Three-dimensional integrated stretchable electronics. *Nat. Electron.* **1**, 473–480 (2018).
32. Gharibans, A. A. et al. Artifact rejection methodology enables continuous, noninvasive measurement of gastric myoelectric activity in ambulatory subjects. *Sci. Rep.* **8**, 5019 (2018).
33. Searle, A. & Kirkup, L. A direct comparison of wet, dry and insulating bioelectric recording electrodes. *Physiol. Meas.* **21**, 271–283 (2000).
34. Krieger, K. J. et al. Development and evaluation of 3D-printed dry microneedle electrodes for surface electromyography. *Adv. Mat. Technol.* **5**, 2000518 (2020).
35. Lee, S. & Kruse, J. Biopotential electrode sensors in ECG/EEG/EMG systems. *Analog Devices* https://www.analog.com/en/technical-articles/biopotential-electrode-sensors-ecg-eeg-emg.html (2008).
36. Ha, S. et al. in *Wearable Sensors* 2nd edn (ed. Sazonov, E.) 163–199 (Elsevier, 2021).
37. Chi, Y. M., Jung, T.-P. & Cauwenberghs, G. Dry-contact and noncontact biopotential electrodes: methodological review. *IEEE Rev. Biomed. Eng.* **3**, 106–119 (2010).
This review introduces skin–electrode coupling mechanisms and highlights recent developments in dry and non-contact biopotential sensors.
38. Yao, S. & Zhu, Y. Nanomaterial-enabled dry electrodes for electrophysiological sensing: a review. *JOM* **68**, 1145–1155 (2016).
39. Zhang, L. et al. Fully organic compliant dry electrodes self-adhesive to skin for long-term motion-robust epidermal biopotential monitoring. *Nat. Commun.* **11**, 4683 (2020).
40. Rivnay, J. et al. Structural control of mixed ionic and electronic transport in conducting polymers. *Nat. Commun.* **7**, 11287 (2016).
41. Liu, J. et al. A novel dry-contact electrode for measuring electroencephalography signals. *Sens. Actuators A* **294**, 73–80 (2019).
42. Wang, Y. et al. Robust, self-adhesive, reinforced polymeric nanofilms enabling gas-permeable dry electrodes for long-term application. *Proc. Natl Acad. Sci. USA* **118**, e2111904118 (2021).
43. Shad, E. H. T., Molinas, M. & Ytterdal, T. Impedance and noise of passive and active dry eeg electrodes: a review. *IEEE Sens. J.* **20**, 14565–14577 (2020).
44. Lv, J. et al. Printable elastomeric electrodes with sweat-enhanced conductivity for wearables. *Sci. Adv.* **7**, eabg8433 (2021).
45. Ershad, F. et al. Ultra-conformal drawn-on-skin electronics for multifunctional motion artifact-free sensing and point-of-care treatment. *Nat. Commun.* **11**, 3823 (2020).
46. Chen, X. et al. Fabric-substrated capacitive biopotential sensors enhanced by dielectric nanoparticles. *Nano Res.* **14**, 3248–3252 (2021).
47. Forvi, E. et al. Preliminary technological assessment of microneedles-based dry electrodes for biopotential monitoring in clinical examinations. *Sens. Actuators A* **180**, 177–186 (2012).
48. Srivastava, A. K., Bhartia, B., Mukhopadhyay, K. & Sharma, A. Long term biopotential recording by body conformable photolithography fabricated low cost polymeric microneedle arrays. *Sens. Actuators A* **236**, 164–172 (2015).
49. Dabbagh, S. R. et al. 3D-printed microneedles in biomedical applications. *Iscience* **24**, 102012 (2020).
50. Hedrich, T., Pellegrino, G., Kobayashi, E., Lina, J.-M. & Grova, C. Comparison of the spatial resolution of source imaging techniques in high-density EEG and MEG. *Neuroimage* **157**, 531–544 (2017).
51. Wang, K. et al. Stretchable dry electrodes with concentric ring geometry for enhancing spatial resolution in electrophysiology. *Adv. Healthc. Mater.* **6**, 1700552 (2017).
52. Makeyev, O. & Besio, W. G. Improving the accuracy of Laplacian estimation with novel variable inter-ring distances concentric ring electrodes. *Sensors* **16**, 858 (2016).
53. Victorino, J. A. et al. Imbalances in regional lung ventilation: a validation study on electrical impedance tomography. *Am. J. Respir. Crit. Care Med.* **169**, 791–800 (2004).
54. Isaacson, D., Mueller, J. L., Newell, J. C. & Siltanen, S. Imaging cardiac activity by the D-bar method for electrical impedance tomography. *Physiol. Meas.* **27**, S43–S50 (2006).
55. Soni, N. K., Hartov, A., Kogel, C., Poplack, S. P. & Paulsen, K. D. Multi-frequency electrical impedance tomography of the breast: new clinical results. *Physiol. Meas.* **25**, 301 (2004).
56. Tidswell, T., Gibson, A., Bayford, R. H. & Holder, D. S. Three-dimensional electrical impedance tomography of human brain activity. *Neuroimage* **13**, 283–294 (2001).
57. Cheney, M., Isaacson, D. & Newell, J. C. Electrical impedance tomography. *SIAM Rev.* **41**, 85–101 (1999).
58. Khan, T. A. & Ling, S. H. Review on electrical impedance tomography: artificial intelligence methods and its applications. *Algorithms* **12**, 88 (2019).
59. Barth, A., Harrach, B., Hyvönen, N. & Mustonen, L. Detecting stochastic inclusions in electrical impedance tomography. *Inverse Probl.* **33**, 115012 (2017).
60. Kelley, C. T. *Solving Nonlinear Equations with Newton's Method* (SIAM, 2003).
61. Adler, A. & Holder, D. S. *Electrical Impedance Tomography: Methods, History and Applications* (CRC, 2004).
This book describes the background science, reconstruction principles and clinical applications of electrical impedance tomography.
62. Yan, W., Hong, S. & Chaoshi, R. Optimum design of electrode structure and parameters in electrical impedance tomography. *Physiol. Meas.* **27**, 291–306 (2006).
63. Rezanejad Gatabi, Z., Mohammadpour, R., Rezanejad Gatabi, J., Mirhoseini, M. & Sasanpour, P. A novel composite gold/gold nanoparticles/carbon nanotube electrode for frequency-stable micro-electrical impedance tomography. *J. Mater. Sci. Mater. Electron.* **31**, 10803–10810 (2020).
64. Oh, T. I. et al. Flexible electrode belt for EIT using nanofiber web dry electrodes. *Physiol. Meas.* **33**, 1603–1616 (2012).
65. Zhang, X. & Zhong, Y. A silver/silver chloride woven electrode with convex based on electrical impedance tomography. *J. Text. Inst.* **112**, 1067–1079 (2021).
66. de Castro Martins, T. et al. A review of electrical impedance tomography in lung applications: theory and algorithms for absolute images. *Annu. Rev. Control* **48**, 442–471 (2019).
67. Sola, J. et al. Non-invasive monitoring of central blood pressure by electrical impedance tomography: first experimental evidence. *Med. Biol. Eng. Comput.* **49**, 409–415 (2011).
68. Romsauerova, A. et al. Multi-frequency electrical impedance tomography (EIT) of the adult human head: initial findings in brain tumours, arteriovenous malformations and chronic stroke, development of an analysis method and calibration. *Physiol. Meas.* **27**, S147 (2006).
69. Wang, Q. et al. Exploring respiratory motion tracking through electrical impedance tomography. *IEEE Trans. Instrum. Meas.* **70**, 1–12 (2021).
70. Metherall, P., Barber, D. C., Smallwood, R. H. & Brown, B. H. Three-dimensional electrical impedance tomography. *Nature* **380**, 509–512 (1996).
71. Graham, B. & Adler, A. Electrode placement configurations for 3D EIT. *Physiol. Meas.* **28**, S29–S44 (2007).
72. Lipani, L. et al. Non-invasive, transdermal, path-selective and specific glucose monitoring via a graphene-based platform. *Nat. Nanotechnol.* **13**, 504–511 (2018).
This article describes an electrode array with millimetre-sized elements for glucose monitoring, which significantly improves the spatial resolution of reverse iontophoresis.
73. Jain, S. M., Pandey, K., Lahoti, A. & Rao, P. K. Evaluation of skin and subcutaneous tissue thickness at insulin injection sites in Indian, insulin naïve, type-2 diabetic adult population. *Indian J. Endocrinol. Metab.* **17**, 864–870 (2013).
74. Yang, Y. & Gao, W. Wearable and flexible electronics for continuous molecular monitoring. *Chem. Soc. Rev.* **48**, 1465–1491 (2019).
75. Bandodkar, A. J. et al. Tattoo-based noninvasive glucose monitoring: a proof-of-concept study. *Anal. Chem.* **87**, 394–398 (2015).
76. Sieg, A., Guy, R. H. & Delgado-Charro, M. B. Electroosmosis in transdermal iontophoresis: implications for noninvasive and calibration-free glucose monitoring. *Biophys. J.* **87**, 3344–3350 (2004).
77. Chen, Y. et al. Skin-like biosensor system via electrochemical channels for noninvasive blood glucose monitoring. *Sci. Adv.* **3**, e1701629 (2017).
78. Gowers, S. A. et al. Development of a minimally invasive microneedle-based sensor for continuous monitoring of β-lactam antibiotic concentrations in vivo. *ACS Sens.* **4**, 1072–1080 (2019).
79. Yang, B., Fang, X. & Kong, J. Engineered microneedles for interstitial fluid cell-free DNA capture and sensing using iontophoretic dual-extraction wearable patch. *Adv. Funct. Mater.* **30**, 2000591 (2020).
80. Wang, Z. et al. Microneedle patch for the ultrasensitive quantification of protein biomarkers in interstitial fluid. *Nat. Biomed. Eng.* **5**, 64–76 (2021).
81. Lee, C.-K. et al. Non-invasive and transdermal measurement of blood uric acid level in human by electroporation and reverse iontophoresis. *Int. J. Nanomed.* **5**, 991–997 (2010).
82. Cengiz, E. & Tamborlane, W. V. A tale of two compartments: interstitial versus blood glucose monitoring. *Diabetes Technol. Ther.* **11**, S-11–S-16 (2009).
83. Giri, T. K., Chakrabarty, S. & Ghosh, B. Transdermal reverse iontophoresis: a novel technique for therapeutic drug monitoring. *J. Control. Release* **246**, 30–38 (2017).
84. Gade, R. & Moeslund, T. B. Thermal cameras and applications: a survey. *Mach. Vis. Appl.* **25**, 245–262 (2014).
85. Carpes, F. P. et al. Insights on the use of thermography in human physiology practical classes. *Adv. Physiol. Educ.* **42**, 521–525 (2018).
86. Best, S. R. in *2011 International Workshop on Antenna Technology* 90–93 (IEEE, 2011).
87. Rossmann, C. & Haemmerich, D. Review of temperature dependence of thermal properties, dielectric properties, and perfusion of biological

tissues at hyperthermic and ablation temperatures. *Crit. Rev. Biomed. Eng.* **42**, 467–492 (2014).
88. Chen, L. Y. et al. Continuous wireless pressure monitoring and mapping with ultra-small passive sensors for health monitoring and critical care. *Nat. Commun.* **5**, 5028 (2014).
89. Roshni, S. B., Jayakrishnan, M., Mohanan, P. & Surendran, K. P. Design and fabrication of an E-shaped wearable textile antenna on PVB-coated hydrophobic polyester fabric. *Smart Mater. Struct.* **26**, 105011 (2017).
90. Wang, Y. et al. Flexible RFID tag metal antenna on paper-based substrate by inkjet printing technology. *Adv. Funct. Mater.* **29**, 1902579 (2019).
91. Tsolis, A., Whittow, W. G., Alexandridis, A. A. & Vardaxoglou, J. Embroidery and related manufacturing techniques for wearable antennas: challenges and opportunities. *Electronics* **3**, 314–338 (2014).
92. Cluff, K. et al. Passive wearable skin patch sensor measures limb hemodynamics based on electromagnetic resonance. *IEEE Trans. Biomed. Eng.* **65**, 847–856 (2017).
93. Stauffer, P. R. et al. Stable microwave radiometry system for long term monitoring of deep tissue temperature. *Proc. SPIE Int. Soc. Opt. Eng.* **8584**, 227–237 (2013).
94. Costanzo, S. & Cioffi, V. in *Information Technology and Systems. ICITS 2020* (eds Rocha, Á. et al.) 607–612 (Springer, 2020).
95. El Gharbi, M., Fernández-Garcîa, R., Ahyoud, S. & Gil, I. A review of flexible wearable antenna sensors: design, fabrication methods, and applications. *Materials* **13**, 3781 (2020).
96. Lee, J. et al. Neural recording and stimulation using wireless networks of microimplants. *Nat. Electron.* **4**, 604–614 (2021).
97. Dong, Z., Li, Z., Yang, F., Qiu, C.-W. & Ho, J. S. Sensitive readout of implantable microsensors using a wireless system locked to an exceptional point. *Nat. Electron.* **2**, 335–342 (2019).
98. Boutry, C. M. et al. Biodegradable and flexible arterial-pulse sensor for the wireless monitoring of blood flow. *Nat. Biomed. Eng.* **3**, 47–57 (2019).
99. Yoo, S. et al. Wireless power transfer and telemetry for implantable bioelectronics. *Adv. Healthc. Mater.* **10**, 2100614 (2021).
This review introduces approaches to retrieve deep-tissue signals and deliver power using wearable antennas and electromagnetic transmission.
100. Karimi, M. J., Schmid, A. & Dehollain, C. Wireless power and data transmission for implanted devices via inductive links: a systematic review. *IEEE Sens. J.* **21**, 7145–7161 (2021).
101. Gutruf, P. et al. Fully implantable optoelectronic systems for battery-free, multimodal operation in neuroscience research. *Nat. Electron.* **1**, 652–660 (2018).
102. Laqua, D., Just, T. & Husar, P. in *2010 Annual International Conference of the IEEE Engineering in Medicine and Biology* 1437–1440 (IEEE, 2010).
103. Burton, A. et al. Wireless, battery-free, and fully implantable electrical neurostimulation in freely moving rodents. *Microsyst. Nanoeng.* **7**, 62 (2021).
104. Ausra, J. et al. Wireless, battery-free, subdermally implantable platforms for transcranial and long-range optogenetics in freely moving animals. *Proc. Natl Acad. Sci. USA* **118**, e2025775118 (2021).
105. Agrawal, D. R. et al. Conformal phased surfaces for wireless powering of bioelectronic microdevices. *Nat. Biomed. Eng.* **1**, 0043 (2017).
106. Lee, J. et al. in *2018 IEEE Biomedical Circuits and Systems Conference* (IEEE, 2018).
107. Bahramiabarghouei, H. et al. Flexible 16 antenna array for microwave breast cancer detection. *IEEE Trans. Biomed. Eng.* **62**, 2516–2525 (2015).
108. Zhang, H. et al. Wireless, battery-free optoelectronic systems as subdermal implants for local tissue oximetry. *Sci. Adv.* **5**, eaaw0873 (2019).
109. Tremper, K. K. Pulse oximetry. *Chest* **95**, 713–715 (1989).
110. Weissleder, R. & Ntziachristos, V. Shedding light onto live molecular targets. *Nat. Med.* **9**, 123–128 (2003).
111. Cohen, L., Salzberg, B. & Grinvald, A. Optical methods for monitoring neuron activity. *Annu. Rev. Neurosci.* **1**, 171–182 (1978).
112. Anderson, R. R. & Parrish, J. A. The optics of human skin. *J. Invest. Dermatol.* **77**, 13–19 (1981).
113. Zonios, G. et al. Melanin absorption spectroscopy: new method for noninvasive skin investigation and melanoma detection. *J. Biomed. Opt.* **13**, 014017 (2008).
114. Lister, T., Wright, P. A. & Chappell, P. H. Optical properties of human skin. *J. Biomed. Opt.* **17**, 90901 (2012).
115. Maeda, Y., Sekine, M. & Tamura, T. The advantages of wearable green reflected photoplethysmography. *J. Med. Syst.* **35**, 829–834 (2011).
116. Maruo, K., Tsurugi, M., Tamura, M. & Ozaki, Y. In vivo noninvasive measurement of blood glucose by near-infrared diffuse-reflectance spectroscopy. *Appl. Spectrosc.* **57**, 1236–1244 (2003).
117. Higurashi, E., Sawada, R. & Ito, T. An integrated laser blood flowmeter. *J. Light. Technol.* **21**, 591–595 (2003).
118. Zhang, H. et al. Biocompatible light guide-assisted wearable devices for enhanced UV light delivery in deep skin. *Adv. Funct. Mater.* **31**, 2100576 (2021).
119. Temko, A. Accurate heart rate monitoring during physical exercises using PPG. *IEEE Trans. Biomed. Eng.* **64**, 2016–2024 (2017).
120. Kim, J. et al. Battery-free, stretchable optoelectronic systems for wireless optical characterization of the skin. *Sci. Adv.* **2**, e1600418 (2016).
121. Lázaro, J., Gil, E., Bailón, R., Mincholé, A. & Laguna, P. Deriving respiration from photoplethysmographic pulse width. *Med. Biol. Eng. Comput.* **51**, 233–242 (2013).
122. Avci, P. et al. Low-level laser (light) therapy (LLLT) in skin: stimulating, healing, restoring. *Semin. Cutan. Med. Surg.* **32**, 41–52 (2013).
123. Mickle, A. D. et al. A wireless closed-loop system for optogenetic peripheral neuromodulation. *Nature* **565**, 361–365 (2019).
124. Choi, S. et al. Highly flexible and efficient fabric-based organic light-emitting devices for clothing-shaped wearable displays. *Sci. Rep.* **7**, 6424 (2017).
125. Kim, J.-H. & Park, J.-W. Intrinsically stretchable organic light-emitting diodes. *Sci. Adv.* **7**, eabd9715 (2021).
126. Ash, C., Dubec, M., Donne, K. & Bashford, T. Effect of wavelength and beam width on penetration in light-tissue interaction using computational methods. *Lasers Med. Sci.* **32**, 1909–1918 (2017).
127. Okamoto, K. *Fundamentals of Optical Waveguides* (Academic, 2006).
128. Shabahang, S., Kim, S. & Yun, S. H. Light-guiding biomaterials for biomedical applications. *Adv. Funct. Mater.* **28**, 1706635 (2018).
129. Choi, M. et al. Light-guiding hydrogels for cell-based sensing and optogenetic synthesis in vivo. *Nat. Photonics* **7**, 987–994 (2013).
130. Chung, S. H., Mehta, R., Tromberg, B. J. & Yodh, A. G. Non-invasive measurement of deep tissue temperature changes caused by apoptosis during breast cancer neoadjuvant chemotherapy: a case study. *J. Innov. Opt. Health Sci.* **4**, 361–372 (2011).
131. Pesonen, E. et al. The focus of temperature monitoring with zero-heat-flux technology (3M Bair-Hugger): a clinical study with patients undergoing craniotomy. *J. Clin. Monit. Comput.* **33**, 917–923 (2019).
132. Gao, X. et al. A photoacoustic patch for three-dimensional imaging of hemoglobin and core temperature. Preprint at *Research Square* https://doi.org/10.21203/rs.3.rs-558432/v1 (2021).
133. Tian, L. et al. Flexible and stretchable 3ω sensors for thermal characterization of human skin. *Adv. Funct. Mater.* **27**, 1701282 (2017).
This article reports a stretchable device using thermal modulation to interrogate tissue conductivity.
134. Qiu, L., Ouyang, Y., Feng, Y., Zhang, X. & Wang, X. In vivo skin thermophysical property testing technology using flexible thermosensor-based 3ω method. *Int. J. Heat Mass Transf.* **163**, 120550 (2020).
135. Hattori, Y. et al. Multifunctional skin-like electronics for quantitative, clinical monitoring of cutaneous wound healing. *Adv. Healthc. Mater.* **3**, 1597–1607 (2014).
136. Kurz, A. Physiology of thermoregulation. *Best Pract. Res. Clin. Anaesthesiol.* **22**, 627–644 (2008).
137. Lim, C. L., Byrne, C. & Lee, J. K. Human thermoregulation and measurement of body temperature in exercise and clinical settings. *Ann. Acad. Med. Singap.* **37**, 347 (2008).
138. Yamakage, M. & Namiki, A. Deep temperature monitoring using a zero-heat-flow method. *J. Anesthesia* **17**, 108–115 (2003).
139. Huang, M., Tamura, T., Chen, W. & Kanaya, S. Evaluation of structural and thermophysical effects on the measurement accuracy of deep body thermometers based on dual-heat-flux method. *J. Therm. Biol.* **47**, 26–31 (2015).
140. Feng, J., Zhou, C., He, C., Li, Y. & Ye, X. Development of an improved wearable device for core body temperature monitoring based on the dual heat flux principle. *Physiol. Meas.* **38**, 652 (2017).
141. Huang, M., Tamura, T., Tang, Z., Chen, W. & Kanaya, S. Structural optimization of a wearable deep body thermometer: from theoretical simulation to experimental verification. *J. Sensors* **2016**, 4828093 (2016).
142. Zhang, Y. et al. Theoretical and experimental studies of epidermal heat flux sensors for measurements of core body temperature. *Adv. Healthc. Mater.* **5**, 119–127 (2016).
143. West, N., Cooke, E., Morse, D., Merchant, R. N. & Görges, M. Zero-heat-flux core temperature monitoring system: an observational secondary analysis to evaluate agreement with naso-/oropharyngeal probe during anesthesia. *J. Clin. Monit. Comput.* **34**, 1121–1129 (2019).
144. Brajkovic, D. & Ducharme, M. B. Confounding factors in the use of the zero-heat-flow method for non-invasive muscle temperature measurement. *Eur. J. Appl. Physiol.* **94**, 386–391 (2005).
145. Fang, J., Zhou, C. & Ye, X. in *IOP Conference Series: Materials Science and Engineering* Vol. 667 (IOP, 2019).
146. Shi, Y. et al. Functional soft composites as thermal protecting substrates for wearable electronics. *Adv. Funct. Mater.* **29**, 1905470 (2019).
147. Dames, C. & Chen, G. 1ω, 2ω, and 3ω methods for measurements of thermal properties. *Rev. Sci. Instrum.* **76**, 124902 (2005).
148. Wang, H. & Sen, M. Analysis of the 3-omega method for thermal conductivity measurement. *Int. J. Heat Mass Transf.* **52**, 2102–2109 (2009).
149. Dagdeviren, C. et al. Conformal piezoelectric energy harvesting and storage from motions of the heart, lung, and diaphragm. *Proc. Natl Acad. Sci. USA* **111**, 1927–1932 (2014).
150. Cotur, Y. et al. Stretchable composite acoustic transducer for wearable monitoring of vital signs. *Adv. Funct. Mater.* **30**, 1910288 (2020).
151. Wang, F. et al. A flexible skin-mounted wireless acoustic device for bowel sounds monitoring and evaluation. *Sci. China Inf. Sci.* **62**, 202402 (2019).
152. Bosco, C. et al. Adaptive respsonses of human skeletal muscle to vibration exposure. *Clin. Physiol.* **19**, 183–187 (1999).
153. Tao, L. Q. et al. An intelligent artificial throat with sound-sensing ability based on laser induced graphene. *Nat. Commun.* **8**, 14579 (2017).
154. Li, W. et al. Nanogenerator-based dual-functional and self-powered thin patch loudspeaker or microphone for flexible electronics. *Nat. Commun.* **8**, 15310 (2017).
155. Song, E. et al. Miniaturized electromechanical devices for the characterization of the biomechanics of deep tissue. *Nat. Biomed. Eng.* **5**, 759–771 (2021).
156. Dagdeviren, C. et al. Conformal piezoelectric systems for clinical and experimental characterization of soft tissue biomechanics. *Nat. Mater.* **14**, 728–736 (2015).
157. Fan, X. et al. Ultrathin, rollable, paper-based triboelectric nanogenerator for acoustic energy harvesting and self-powered sound recording. *ACS Nano* **9**, 4236–4243 (2015).
158. Lee, H. S. et al. Flexible inorganic piezoelectric acoustic nanosensors for biomimetic artificial hair cells. *Adv. Funct. Mater.* **24**, 6914–6921 (2014).
159. Nayeem, M. O. G. et al. All-nanofiber-based, ultrasensitive, gas-permeable mechanoacoustic sensors for continuous long-term heart monitoring. *Proc. Natl Acad. Sci. USA* **117**, 7063–7070 (2020).
This article describes an ultrasensitive, nanofibre-based, passive vibration sensor for continuous cardiac sensing.
160. Gupta, P., Wen, H., Di Francesco, L. & Ayazi, F. Detection of pathological mechano-acoustic signatures using precision accelerometer contact microphones in patients with pulmonary disorders. *Sci. Rep.* **11**, 13427 (2021).
161. Hu, Y. & Xu, Y. in *2012 Annual International Conference of the IEEE Engineering in Medicine and Biology Society* 694–697 (IEEE, 2012).
162. Lee, K. et al. Mechano-acoustic sensing of physiological processes and body motions via a soft wireless device placed at the suprasternal notch. *Nat. Biomed. Eng.* **4**, 148–158 (2020).
163. Liu, Y. et al. Epidermal mechano-acoustic sensing electronics for cardiovascular diagnostics and human-machine interfaces. *Sci. Adv.* **2**, e1601185 (2016).

164. Gupta, P. et al. Precision wearable accelerometer contact microphones for longitudinal monitoring of mechano-acoustic cardiopulmonary signals. *NPJ Digit. Med.* **3**, 19 (2020).
165. Yang, C. & Tavassolian, N. An independent component analysis approach to motion noise cancelation of cardio-mechanical signals. *IEEE Trans. Biomed. Eng.* **66**, 784–793 (2018).
166. Yu, X. et al. Needle-shaped ultrathin piezoelectric microsystem for guided tissue targeting via mechanical sensing. *Nat. Biomed. Eng.* **2**, 165–172 (2018).
167. Yu, X. et al. Skin-integrated wireless haptic interfaces for virtual and augmented reality. *Nature* **575**, 473–479 (2019).
168. Maccabi, A. et al. Quantitative characterization of viscoelastic behavior in tissue-mimicking phantoms and ex vivo animal tissues. *PLoS ONE* **13**, e0191919 (2018).
169. Shung, K. K. *Diagnostic Ultrasound: Imaging and Blood Flow Measurements* (CRC, 2005).
170. Hu, H. et al. Stretchable ultrasonic transducer arrays for three-dimensional imaging on complex surfaces. *Sci. Adv.* **4**, eaar3979 (2018).
This article reports a stretchable ultrasound array device that can conform to nondevelopable surfaces for reconstructing 3D structures located deep underneath the surface.
171. Li, Z. et al. Broadband gradient impedance matching using an acoustic metamaterial for ultrasonic transducers. *Sci. Rep.* **7**, 42863 (2017).
172. Huang, H. & Paramo, D. Broadband electrical impedance matching for piezoelectric ultrasound transducers. *IEEE Trans. Ultrason. Ferroelectr. Freq. Control* **58**, 2699–2707 (2011).
173. Wang, C. et al. Continuous monitoring of deep-tissue haemodynamics with stretchable ultrasonic phased arrays. *Nat. Biomed. Eng.* **5**, 749–758 (2021).
This article introduces the design of a skin-conformal ultrasonic phased array to sense haemodynamic signals in deep tissue.
174. Roy, O., Mahaut, S. & Casula, O. in *AIP Conference Proceedings* 908–914 (American Institute of Physics, 2002).
175. Frankle, R. S. & Rose, D. N. in *Nondestructive Evaluation of Aging Maritime Applications* 51–59 (SPIE, 1995).
176. Wang, C. et al. Monitoring of the central blood pressure waveform via a conformal ultrasonic device. *Nat. Biomed. Eng.* **2**, 687–695 (2018).
177. Sempionatto, J. R. et al. An epidermal patch for the simultaneous monitoring of haemodynamic and metabolic biomarkers. *Nat. Biomed. Eng.* **5**, 737–748 (2021).
178. Peng, C., Chen, M., Sim, H. K., Zhu, Y. & Jiang, X. in *15th International Conference on Nano/Micro Engineered and Molecular System* 143–146 (IEEE, 2020).
179. AlMohimeed, I., Turkistani, H. & Ono, Y. In *2013 IEEE International Ultrasonics Symposium* 1137–1140 (IEEE, 2013).
180. Pang, D.-C. & Chang, C.-M. Development of a novel transparent flexible capacitive micromachined ultrasonic transducer. *Sensors* **17**, 1443 (2017).
181. Powell, D. & Hayward, G. Flexible ultrasonic transducer arrays for nondestructive evaluation applications. II. Performance assessment of different array configurations. *IEEE Trans. Ultrason. Ferroelectr. Freq. Control* **43**, 393–402 (1996).
182. Li, Z., Chen, A. I., Wong, L. L., Na, S. & Yeow, J. T. in *2015 IEEE International Ultrasonics Symposium* (IEEE, 2015).
183. Qiu, Y. et al. Piezoelectric micromachined ultrasound transducer (PMUT) arrays for integrated sensing, actuation and imaging. *Sensors* **15**, 8020–8041 (2015).
184. Lee, J.-H. et al. Flexible piezoelectric micromachined ultrasonic transducer (pMUT) for application in brain stimulation. *Microsyst. Technol.* **23**, 2321–2328 (2017).
185. Duval, F. F., Dorey, R. A., Wright, R. W., Huang, Z. & Whatmore, R. W. Fabrication and modeling of high-frequency PZT composite thick film membrance resonators. *IEEE Trans. Ultrason. Ferroelectr. Freq. Control* **51**, 1255–1261 (2004).
186. Bowen, C., Bradley, L., Almond, D. & Wilcox, P. Flexible piezoelectric transducer for ultrasonic inspection of non-planar components. *Ultrasonics* **48**, 367–375 (2008).
187. Pashaei, V. et al. Flexible body-conformal ultrasound patches for image-guided neuromodulation. *IEEE Trans. Biomed. Circuits Syst.* **14**, 305–318 (2019).
188. Kato, Y. et al. Large-area flexible ultrasonic imaging system with an organic transistor active matrix. *IEEE Trans. Electron. Devices* **57**, 995–1002 (2010).
189. Chen, Z. et al. High-frequency ultrasonic imaging with lead-free (Na,K)(Nb,Ta)O_3 single crystal. *Ultrason. Imaging* **39**, 348–356 (2017).
190. Hettiarachchi, N., Ju, Z. & Liu, H. in *2015 IEEE International Conference on Systems, Man, and Cybernetics* 1415–1420 (IEEE, 2017).
191. Yang, X., Yan, J. & Liu, H. Comparative analysis of wearable a-mode ultrasound and SEMG for muscle-computer interface. *IEEE Trans. Biomed. Eng.* **67**, 2434–2442 (2019).
192. Stadler, R. W., Taylor, J. A. & Lees, R. S. Comparison of B-mode, M-mode and echo-tracking methods for measurement of the arterial distension waveform. *Ultrasound Med. Biol.* **23**, 879–887 (1997).
193. Shung, K. K. *Diagnostic Ultrasound: Imaging and Blood Flow Measurements* (CRC, 2005).
194. Ding, H. et al. A pulsed wave Doppler ultrasound blood flowmeter by PMUTs. *J. Microelectromech. Syst.* **30**, 680–682 (2021).
195. Jiang, J. & Hall, T. J. A coupled subsample displacement estimation method for ultrasound-based strain elastography. *Phys. Med. Biol.* **60**, 8347 (2015).
196. Kallel, F. & Ophir, J. A least-squares strain estimator for elastography. *Ultrason. Imaging* **19**, 195–208 (1997).
197. Francois Dord, J. et al. in *Ultrasound Elastography for Biomedical Applications and Medicine* (eds Nenadic, I. Z. et al.) 129–142 (Wiley, 2018).
198. Papadacci, C., Bunting, E. A. & Konofagou, E. E. 3D quasi-static ultrasound elastography with plane wave in vivo. *IEEE Trans. Med. Imaging* **36**, 357–365 (2016).
199. Alam, S. K., Ophir, J. & Varghese, T. Elastographic axial resolution criteria: an experimental study. *IEEE Trans. Ultrason. Ferroelectr. Freq. Control* **47**, 304–309 (2000).
200. Ramalli, A., Basset, O., Cachard, C., Boni, E. & Tortoli, P. Frequency-domain-based strain estimation and high-frame-rate imaging for quasi-static elastography. *IEEE Trans. Ultrason. Ferroelectr. Freq. Control* **59**, 817–824 (2012).
201. Chen, H., Varghese, T., Rahko, P. S. & Zagzebski, J. Ultrasound frame rate requirements for cardiac elastography: experimental and in vivo results. *Ultrasonics* **49**, 98–111 (2009).
202. Schrank, F. et al. Real-time MR elastography for viscoelasticity quantification in skeletal muscle during dynamic exercises. *Magn. Reson. Med.* **84**, 103–114 (2020).
203. Fink, M. Time reversal of ultrasonic fields. I. Basic principles. *IEEE Trans. Ultrason. Ferroelectr. Freq. Control* **39**, 555–566 (1992).
204. Turner, B. L. et al. Ultrasound-powered implants: a critical review of piezoelectric material selection and applications. *Adv. Healthc. Mater.* **10**, 2100986 (2021).
205. Sonmezoglu, S., Fineman, J. R., Maltepe, E. & Maharbiz, M. M. Monitoring deep-tissue oxygenation with a millimeter-scale ultrasonic implant. *Nat. Biotechnol.* **39**, 855–864 (2021).
206. Shi, C., Costa, T., Elloian, J., Zhang, Y. & Shepard, K. L. A 0.065-mm^3 monolithically-integrated ultrasonic wireless sensing mote for real-time physiological temperature monitoring. *IEEE Trans. Biomed. Circuits Syst.* **14**, 412–424 (2020).
207. Weber, M. J. et al. A miniaturized single-transducer implantable pressure sensor with time-multiplexed ultrasonic data and power links. *IEEE J. Solid-State Circuits* **53**, 1089–1101 (2018).
208. Jin, P. et al. A flexible, stretchable system for simultaneous acoustic energy transfer and communication. *Sci. Adv.* **7**, eabg2507 (2021).
209. Lyu, W. et al. Flexible ultrasonic patch for accelerating chronic wound healing. *Adv. Healthc. Mater.* **10**, 2100785 (2021).
210. Zhou, H. et al. Wearable ultrasound improves motor function in an MPTP mouse model of Parkinson's disease. *IEEE Trans. Biomed. Eng.* **66**, 3006–3013 (2019).
211. Xu, S. Closed-loop actuating and sensing epidermal systems. US Patent 16/093,820 (2017).
212. Manohar, S. & Razansky, D. Photoacoustics: a historical review. *Adv. Opt. Photonics* **8**, 586–617 (2016).
213. & Lin, J. C. Microwave thermoacoustic tomographic (MTT) imaging. *Phys. Med. Biol.* **66**, 10TR02 (2021).
214. Hin, J. et al. A flexible optoacoustic blood stethoscope for non-invasive multiparametric cardiovascular monitoring. Preprint at *Research Square* https://doi.org/10.21203/rs.3.rs-384531/v1 (2021).
215. Borcea, L. Electrical impedance tomography. *Inverse Probl.* **18**, R99–R126 (2002).
216. Jibiki, T. Coded excitation medical ultrasound imaging. *Igaku Butsuri* **21**, 136–141 (2001).
217. Isla, J. & Cegla, F. Coded excitation for pulse-echo systems. *IEEE Trans. Ultrason. Ferroelectr. Freq. Control* **64**, 736–748 (2017).
218. Beniczky, S., Karoly, P., Nurse, E., Ryvlin, P. & Cook, M. Machine learning and wearable devices of the future. *Epilepsia* **62**, S116–S124 (2021).
219. Jaber, M. S. H. & Kazemi, A. Noise reduction of signals received from wearable sensors along with integrating their information with machine learning. *EurAsian J. Biosci.* **14**, 5253–5259 (2020).
220. Zhang, B., Sodickson, D. K. & Cloos, M. A. A high-impedance detector-array glove for magnetic resonance imaging of the hand. *Nat. Biomed. Eng.* **2**, 570–577 (2018).
221. Wang, J. et al. in *2020 IEEE Symposium on VLSI Circuits* (IEEE, 2020).
222. Chen, K., Lee, H.-S. & Sodini, C. G. in *2014 Symposium on VLSI Circuits Digest of Technical Papers* (IEEE, 2014).
223. Biggs, J. et al. A natively flexible 32-bit Arm microprocessor. *Nature* **595**, 532–536 (2021).
224. Wang, S. et al. Skin electronics from scalable fabrication of an intrinsically stretchable transistor array. *Nature* **555**, 83–88 (2018).
225. Lee, Y., Cha, S. H., Kim, Y.-W., Choi, D. & Sun, J.-Y. Transparent and attachable ionic communicators based on self-cleanable triboelectric nanogenerators. *Nat. Commun.* **9**, 1804 (2018).
226. Niu, S. et al. A wireless body area sensor network based on stretchable passive tags. *Nat. Electron.* **2**, 361–368 (2019).
227. Lin, M., Gutierrez, N.-G. & Xu, S. Soft sensors form a network. *Nat. Electron.* **2**, 327–328 (2019).
228. Li, Z., Tian, X., Qiu, C.-W. & Ho, J. S. Metasurfaces for bioelectronics and healthcare. *Nat. Electron.* **4**, 382–391 (2021).
229. Tian, X. et al. Wireless body sensor networks based on metamaterial textiles. *Nat. Electron.* **2**, 243–251 (2019).
230. Lim, C. et al. Tissue-like skin-device interface for wearable bioelectronics by using ultrasoft, mass-permeable, and low-impedance hydrogels. *Sci. Adv.* **7**, eabd3716 (2021).
231. Huang, D., Wang, H., Li, J., Chen, Y. & Li, Z. in *20th International Conference on Solid-State Sensors, Actuators and Microsystems & Eurosensors* 298–301 (IEEE, 2019).
232. Liu, J., Jiang, L., Liu, H. & Cai, X. A bifunctional biosensor for subcutaneous glucose monitoring by reverse iontophoresis. *J. Electroanal. Chem.* **660**, 8–13 (2011).
233. Alberto, J. et al. Fully untethered battery-free biomonitoring electronic tattoo with wireless energy harvesting. *Sci. Rep.* **10**, 5539 (2020).
234. Choi, Y. S. et al. Fully implantable and bioresorbable cardiac pacemakers without leads or batteries. *Nat. Biotechnol.* **39**, 1228–1238 (2021).
235. Choi, M., Humar, M., Kim, S. & Yun, S. H. Step-index optical fiber made of biocompatible hydrogels. *Adv. Mater.* **27**, 4081–4086 (2015).
236. Schröder, H. et al. in *Optoelectronic Integrated Circuits VIII* 612407 (SPIE, 2006).
237. Manocchi, A. K., Domachuk, P., Omenetto, F. G. & Yi, H. Facile fabrication of gelatin-based biopolymeric optical waveguides. *Biotechnol. Bioeng.* **103**, 725–732 (2009).
238. Hanada, Y., Sugioka, K. & Midorikawa, K. UV waveguides light fabricated in fluoropolymer CYTOP by femtosecond laser direct writing. *Opt. Express* **18**, 446–450 (2010).
239. Liu, C.-H. & Kenny, T. W. A high-precision, wide-bandwidth micromachined tunneling accelerometer. *J. Microelectromech. Syst.* **10**, 425–433 (2001).
240. Zhu, H.-T., Chen, Y., Xiong, Y.-F., Xu, F. & Lu, Y.-Q. A flexible wireless dielectric sensor for noninvasive fluid monitoring. *Sensors* **20**, 174 (2020).
241. Choi, A. & Shin, H. Photoplethysmography sampling frequency: pilot assessment of how low can we go to

analyze pulse rate variability with reliability? *Physiol. Meas.* **38**, 586 (2017).
242. Guschlbauer, M. et al. Zero-heat-flux thermometry for non-invasive measurement of core body temperature in pigs. *PLoS ONE* **11**, e0150759 (2016).
243. Sharma, S., Huang, Z., Rogers, M., Boutelle, M. & Cass, A. E. Evaluation of a minimally invasive glucose biosensor for continuous tissue monitoring. *Anal. Bioanal. Chem.* **408**, 8427–8435 (2016).
244. Ren, L. et al. Fabrication of flexible microneedle array electrodes for wearable bio-signal recording. *Sensors* **18**, 1191 (2018).

Acknowledgements
The authors gratefully acknowledge financial support from the National Institutes of Health grants 1R21EB025521-01, 1R21EB027303-01A1 and 3R21EB027303-02S1. The authors thank S. Xiang for valuable discussions and constructive feedback on manuscript preparation, and all authors whose work is reviewed in this article.

Author contributions
M.L., H.H. and S.Z. contributed equally to the literature review, figure design, manuscript writing and discussion of content. S.X. conceived the article. All authors contributed to reviewing and editing the manuscript.

Competing interests
The authors declare no competing interests.

Peer review statement
Nature Reviews Materials thanks Sei Kwang Hahn and the other, anonymous, reviewers for their contribution to the peer review of this work.

Publisher's note
Springer Nature remains neutral with regard to jurisdictional claims in published maps and institutional affiliations.